Thermal and chemical evolution in the early Solar System as recorded by FUN CAIs: Part I - Petrology, mineral chemistry, and isotopic composition of Allende FUN CAI CMS-1

C. D. Williams[1†*], T. Ushikubo[2 ‡], E. S. Bullock[3 ζ], P. E. Janney[1§], R. R. Hines[1], N. T. Kita[2], R. L. Hervig[1], G. J. MacPherson[3], R. A. Mendybaev[4], F. M. Richter[4], and M. Wadhwa[1].

[1]School of Earth and Space Exploration, Arizona State University, Tempe, AZ 85287, United States

[2]WiscSIMS, Department of Geosciences, University of Wisconsin, Madison, WI 53706, United States

[3]Department of Mineral Sciences, National Museum of Natural History, Smithsonian Institution, Washington, DC 20560, United States

[4]Department of Geophysical Sciences, University of Chicago, Chicago, IL 60637, United States

[†]Current address: Department of Earth and Planetary Sciences, University of California at Davis, Davis, CA 95616

[‡]Current address: Kochi Institute for Core Sample Research, JAMSTEC, 200 Monobe-otsu, Nankoku, Kochi 783-8502 Japan

[ζ]Current address: Geophysical Laboratory, Carnegie Institution for Science, 5251 Broad Branch Road N. W., Washington, DC 20015

[§]Current address: Department of Geological Sciences, University of Cape Town, Private Bag X3, Rondebosch 7701 South Africa

*Corresponding author. Email address: cdwill@ucdavis.edu

To be submitted to Geochimica et Cosmochimica Acta

Abstract

Detailed petrologic, geochemical and isotopic analyses of a new FUN CAI from the Allende CV3 meteorite (designated CMS-1) indicate that it formed by extensive melting and evaporation of primitive precursor material(s). The precursor material(s) condensed in a ^{16}O-rich region (δ^{17}O and δ^{18}O ~ -49‰) of the inner solar nebula dominated by gas of solar composition at total pressures of ~10^{-3} to 10^{-6} bar. Subsequent melting of the precursor material(s) was accompanied by evaporative loss of magnesium, silicon and oxygen resulting in large mass-dependent isotope fractionations in these elements (δ^{25}Mg = 30.71 – 39.26‰, δ^{29}Si = 14.98 – 16.65‰, and δ^{18}O = -41.57 – -15.50‰). This evaporative loss resulted in a bulk composition similar to that of compact Type A and Type B CAIs, but very distinct from the composition of the original precursor condensate(s). Kinetic fractionation factors and the measured mass-dependent fractionation of silicon and magnesium in CMS-1 suggest that ~ 80% of the silicon and ~85% of the magnesium were lost from its precursor material(s) through evaporative processes. These results suggest that the precursor material(s) of normal and FUN CAIs condensed in similar environments, but subsequently evolved under vastly different conditions such as total gas pressure. The chemical and isotopic differences between normal and FUN CAIs could be explained by sorting of early solar system materials into distinct physical and chemical regimes, in conjunction with discrete heating events, within the protoplanetary disk.

1. Introduction

The refractory calcium-aluminum-rich inclusions (CAIs) in chondritic meteorites are the oldest dated solids in the solar system (Amelin et al., 2002; Wadhwa and Bouvier, 2010; Connelly et al., 2012). Many FUN CAIs display textures and bulk compositions similar to those of isotopically normal compact Type A CAIs, Type B CAIs, forsterite-bearing Type B CAIs, and hibonite-rich inclusions (see Krot et al., 2014). The correlated mass-dependent isotopic fractionations of magnesium, silicon and oxygen in normal CAIs (e.g., Grossman et al., 2000, 2008a) are usually attributed to Rayleigh isotope fractionation of these moderately volatile elements as a result of evaporation. Rayleigh fractionation has been found to be responsible for the heavy-isotope enrichment of laboratory evaporation residues when silicate melts are subject to temperatures and pressures consistent with inner nebula conditions in the early solar system (Davis et al., 1990; Hashimoto, 1990; Nagahara and Ozawa, 1996; Richter et al., 2002, 2007; Knight et al., 2009; Mendybaev et al., 2013a,b). The substantial enrichment in the heavy isotopes of silicon and magnesium observed in FUN CAIs (Lee et al., 1976; Clayton and Mayeda, 1977; Clayton et al., 1977, 1978, 1984; Wasserburg et al., 1977; Yeh and Epstein, 1978; Molini-Velsko et al., 1983; Papanastassiou and Brigham, 1989; Davis et al., 1991; Loss et al., 1994; Srinivasan et al., 2000; Thrane et al., 2008; Krot et al., 2014) indicates that a very large portion of their original silicon and magnesium must have evaporated and been lost to the gas phase.

Recently, Mendybaev et al. (2013b) reported the results for a set of experiments in which forsterite-rich starting compositions were melted and evaporated under vacuum (~10^{-9} bar) to varying degrees. The evaporation residues were compared to the reported bulk chemical and isotopic compositions of FUN CAIs Vigarano 1623-5 and C1 (Conard, 1976; Lee et al., 1976; Clayton and

Mayeda, 1977; Clayton et al., 1977; Wasserburg et al., 1977; Molini-Velsko et al., 1983; Loss et al., 1994; Davis et al., 1991, 2000). These results, building upon previous experimental and theoretical considerations (e.g., Davis et al., 1990; Wang et al., 2001; Richter et al., 2002, 2007), established that the present chemical and isotopic compositions of FUN CAIs could be explained by evaporation of precursor material with initial bulk compositions close to those predicted for solids condensing from a gas of solar composition (Grossman et al., 2008a). A new set of evaporation experiments focused on understanding the precursor composition and thermo-chemical evolution of CMS-1 is presented in a companion paper (Mendybaev et al., 2016).

The CMS-1 inclusion was first identified as a FUN CAI on the basis of its titanium isotopic composition (Williams et al., 2016). This current study presents more detailed petrologic, geochemical, and isotopic data for this inclusion. Specifically, we report here mineralogic data, rare earth element compositions, and the isotopic compositions of magnesium, silicon and oxygen in CMS-1. These data demonstrate that the precursor material(s) for this inclusion was characterized by a bulk composition consistent with condensation from a gas of solar composition having perhaps an initial mineral assemblage similar to forsterite-bearing inclusions (FoBs). This assemblage of condensates appears to have been transported to the edge of the protoplanetary disk where it experienced one or more high-temperature heating events that resulted in significant evaporative loss and modification of its bulk chemical and isotopic composition. This study places further constraints on the physical and chemical conditions that prevailed within the protoplanetary disk early in its evolutionary history.

2. Methods

The CMS-1 FUN inclusion was located in a cut slab of the Allende meteorite obtained from the meteorite collection in the Center for Meteorite Studies at Arizona State University (ASU). The inclusion was approximately 3 × 5 mm in overall maximum dimensions (Fig. 1; Suppl. Figs. S1-S3). Major and trace element abundances were acquired in individual minerals in a polished thin section of CMS-1 (prepared from a portion of the inclusion that was split and mounted in epoxy; Suppl. Figs. S4-S5) using the Cameca SX100 Ultra EPMA at the Michael J. Drake Electron Microprobe Laboratory, University of Arizona (UA) and the JEOL JXA-8900 Superprobe at the Smithsonian Institution (SI), Washington D. C. All quantitative analyses using the EMPA instruments at the UA and the SI were conducted with an accelerating potential of 15 kV, 20 nA beam current, and a 1 μm diameter beam. Calibrations were performed for different elements using the following silicate and oxide minerals as standards: diopside (Mg), fayalite (Fe), albite (Na), anorthite (Al), orthoclase (K), rhodonite (Mn), titanite (Si, Ca, and Ti), chromite (Cr) at the UA; Kakanui hornblende (Si, Na, Ti, Fe, K); wollastonite (Si, Ca); olivine (Mg); spinel (Mg and Al); diopside (Mg); bytownite (Al), manganite (Mn) and chromite (Cr) at the SI. Detection limits (in wt. %) for the oxides are as follows: SiO_2 (UA and SI: 0.02), TiO_2 (UA: 0.02, SI: 0.03), Al_2O_3 (UA and SI: 0.02), Cr_2O_3 (UA and SI: 0.02), FeO (UA: 0.05, SI: 0.03), MnO (UA: 0.04, SI: 0.02), MgO (UA and SI: 0.03), CaO (UA and SI: 0.02), Na_2O (UA: 0.02, SI: 0.04), and K_2O (UA and SI: 0.01). Backscattered electron (BSE) and elemental maps of CMS-1 were acquired at both the UA and the SI (Figs. 2-8; Suppl. Figs. S6-S8). At the UA, elemental maps were acquired with the Cameca SX100 Ultra EPMA using a fully focused electron beam. The conditions for acquisition of elemental maps were 15 kV accelerating potential, 100 nA beam current, 10 ms dwell time per pixel, and resolution of ~ 2 μm per pixel using wavelength dispersive spectrometry. The elemental maps were combined using the Peaksight software package. Elemental maps at the SI were

88 obtained using an FEI Nova NanoSEM 600 field emission scanning electron microscope (SEM)
89 operating at 15 kV accelerating potential, 2 nA beam current, with a 1μm beam. Data were
90 collected using a Thermo-Scientific Noran System Six energy dispersive spectrometer system.
91
92 Concentrations of rare earth elements (REE) and additional selected trace elements were measured
93 *in situ* in the CMS-1 thin section using a Cameca IMS-6f secondary ion mass spectrometer (SIMS)
94 at ASU, utilizing the energy filtering technique described by Zinner and Crozaz (1986). Analyses
95 were performed using an O^- primary beam with currents in the range of 3–7 nA and an accelerating
96 voltage of -12.5 keV. Secondary ions were accelerated to +9 keV and only ions with 75±20 eV
97 excess kinetic energy were detected (to minimize interferences from molecular ions). Secondary
98 ions were detected in peak jumping mode using an electron multiplier. Analysis time for an
99 individual measurement was ~40 minutes. The REE and other trace element concentrations were
100 determined by normalizing analyte intensities to those of a reference isotope (silicon for silicates),
101 with these normalized values adjusted using previously determined sensitivity factors (Zinner and
102 Crozaz, 1986). Standards (i.e., NIST-610, NIST-612, NIST-614) were measured at the beginning
103 and regularly throughout the analytical sessions. While energy filtering reduces the interferences
104 due to molecular ions, isobaric interferences by oxides can still occur, particularly the interferences
105 of light rare earth element (LREE) oxides on the heavy rare earth element (HREE) masses (Zinner
106 and Crozaz, 1986). Using previously determined oxide to element ratios at our particular energy
107 filtering conditions and the ion signals of the LREE measured on the SIMS during the analytical
108 sessions, deconvolution of the LREE oxide interferences on the HREE masses was completed
109 using procedures similar to those described previously (Zinner and Crozaz, 1986; Hinton, 1990).
110 Initially, thorium and uranium concentrations were determined by detection of both atomic (Th^+

111 and U^+) and monoxide species (ThO^+ and UO^+) following the methods of Fahey et al. (1987) to
112 confirm that the appropriate peaks were being measured. Subsequent measurements included only
113 the detection of the atomic species.
114
115 Magnesium and silicon isotope ratios measurements were performed on the CMS-1 inclusion in
116 the cut slab of Allende (Fig. 1) by LA-MC-ICPMS using a ThermoFinnigan Neptune instrument
117 in the Isotope Cosmochemistry and Geochronology Laboratory at ASU. Analytical conditions
118 were similar to those described in Janney et al. (2011). Magnesium isotopes ^{24}Mg, ^{25}Mg and ^{26}Mg,
119 as well as ^{27}Al were measured by static multi-collection. Silicon isotopes (^{28}Si, ^{29}Si and ^{30}Si) were
120 also measured in static multi-collection in separate analytical sessions. Magnesium isotope ratios
121 were measured in medium resolution mode, while silicon isotopic measurements were conducted
122 in high-resolution mode. Both magnesium and silicon isotope measurements consisted of
123 approximately 320 s of data acquisition, consisting of forty 8 s integrations. Spot sizes ranged
124 between 69 and 150 μm with a laser repeat rate of 4 Hz conducted at full power (7 mJ/pulse). On-
125 peak gas blanks were acquired while the He carrier and Ar makeup gases were flowing but without
126 the laser firing, and were conducted prior to analysis of standards and samples as well as after
127 every sample change. These blank intensities were subtracted from all sample and standard
128 intensities before ratios were calculated. Typically, gas blank ion currents for ^{24}Mg were less than
129 2.5×10^{-14} A, while gas blank ion currents for ^{28}Si were typically less than 4.0×10^{-13} A. Mass-
130 dependent variations in magnesium ($\delta^{25}Mg$ and $\delta^{26}Mg$) and silicon ($\delta^{29}Si$ and $\delta^{30}Si$ values) isotope
131 ratios are reported in parts per mil relative to the DSM-3 and NBS-28 standards, respectively. The
132 mass-independent variations in the $^{26}Mg/^{24}Mg$ ratio (i.e., $\delta^{26}Mg^*$) were calculated using an
133 exponential law with the coefficient $\beta = 0.5128$ (Davis et al., 2015). Typical external

reproducibilities (2SD) are ±0.1, ±0.2 and ±0.1‰ for $\delta^{25}Mg$, $\delta^{26}Mg$ and $\delta^{26}Mg^*$, respectively, and ±0.1 and ±0.2‰ for $\delta^{29}Si$ and $\delta^{30}Si$, respectively.

The CAMECA IMS1280 SIMS in the WiscSIMS laboratory was also used to perform magnesium isotope ratio measurements on individual phases in the CMS-1 thin section following the procedures of Kita et al. (2012). All analyses were performed in static multi-collection mode using Faraday cups (MC-FC). For MC-FC analyses, a primary O^- ion beam with a total impact energy of 23 kV was adjusted to produce a 10×15 μm oval shape with an ion current of 2 nA (spinel) or 9 nA (melilite and Ti-Al-rich pyroxene). Secondary ions were accelerated at 10 keV and the secondary optics were adjusted to 200 times magnification from the sample to the field aperture (4000 μm^2) with mass resolving power of ~2500 (entrance slit; 90 μm and exit slit 500 μm). The contributions of $^{48}Ca^{++}$ and MgH^+ interferences to the Mg^+ mass spectrum were negligible. The energy slit was set to 40 eV. Four multi-collection FC detectors were used to detect $^{24}Mg^+$, $^{25}Mg^+$, $^{26}Mg^+$ (with 10^{11} ohm resistors) and $^{27}Al^+$ (with 10^{10} ohm resistor) simultaneously, with $^{25}Mg^+$ set to the ion optical axis. Secondary $^{24}Mg^+$ and $^{27}Al^+$ ion intensities were within the ranges (1.4–7.4) × 10^7 and (0.8–1.5) × 10^8 cps (counts per second), respectively, depending on the mineral phase analyzed. Analysis time was 8 minutes total, including 60 s of presputtering, 120 s for automated centering of the secondary optics, and 300 s of integration (10 s x 30 cycles) of the Mg^+ and Al^+ signals. Due to differences in Mg concentrations, we analyzed each mineral type in separate analytical sessions. The bracketing standards included natural spinel and synthetic glasses with compositions equivalent to melilite (~Åk65) and Ti-Al-rich pyroxene with 5 wt.% TiO_2, which were used for the analysis of spinel, melilite and Ti-Al-rich pyroxene, respectively. In addition, multiple synthetic and natural standards for melilite ($Åk_{25}$, $Åk_{35}$, and $Åk_{75}$-glasses) and Ti-Al-rich

157 pyroxene (2 wt.% TiO_2 and 10 wt.% TiO_2-glasses) were used to evaluate the matrix effect of the
158 instrumental bias (Kita et al., 2012). A total of eight standard analyses were obtained that bracketed
159 8–10 unknown sample analyses. The average values of the bracket standard analyses were used to
160 correct for instrumental bias on the measured magnesium isotope ratios. The measured ratios
161 ($^{25}Mg/^{24}Mg$ and $^{26}Mg/^{24}Mg$) are converted to delta notation ($\delta^{25}Mg$ and $\delta^{26}Mg$) relative to the
162 DSM-3 standard by comparing to those of synthetic glass standards with either known $\delta^{25}Mg$
163 values or natural mineral standards that are assumed to be $\delta^{25}Mg=0$ (Kita et al., 2012) though this
164 assumption may not be correct at the sub-per mil level. The matrix effects on Mg isotope ratios
165 (which are entirely mass-dependent) in melilite and Ti-Al-rich pyroxene were estimated from the
166 analyses of multiple standards. In melilite, these matrix effects increase linearly by 1‰ amu^{-1} from
167 $Åk_{25}$ to $Åk_{75}$, while in Ti-Al-rich pyroxene, they decrease linearly by a total of 1‰ amu^{-1} as TiO_2
168 increases from 2 to 10 wt.%. The $\delta^{25}Mg$ values in individual phases of CMS-1 were corrected
169 according to their Åk mole % and TiO_2 wt.% for melilite and Ti-Al-rich pyroxene, respectively.
170 The instrumental bias on $\delta^{25}Mg$ in spinel was estimated by assuming the $\delta^{25}Mg$ value in the
171 standard to be zero. External reproducibility (2SD) of measured $\delta^{25}Mg$ values of standards is
172 typically 0.2‰ for spinel, 0.2–0.4‰ for melilite, and 0.5–0.8‰ for pyroxene. The mass-
173 independent variations in the $^{26}Mg/^{24}Mg$ ratio (i.e., $\delta^{26}Mg^*$) were calculated using an exponential
174 law with the coefficient $\beta = 0.5128$ (Davis et al., 2015).
175
176 Oxygen isotope ratios were also measured in the CMS-1 thin section by multi-collector SIMS
177 using the Cameca IMS 1280 at the WiscSIMS laboratory, University of Wisconsin-Madison.
178 Analytical conditions were similar to those reported in Kita et al. (2009; 2010). A focused Cs^+
179 beam was tuned to produce a 15 μm diameter spot with a primary ion intensity of 3 nA. Secondary

ions of $^{16}O^-$, $^{17}O^-$ and $^{18}O^-$ were detected simultaneously using three Faraday cups, with typical count rates of 3.5×10^9, 1.3×10^6, and 6.9×10^6 cps, respectively. The total integration time was approximately 3.5 minutes. The mass resolving power was set to ~2200 for $^{16}O^-$ and $^{18}O^-$ using two detectors on the multi-collection array and ~5000 for $^{17}O^-$ using the axial detector at a fixed position. After each analysis, $^{16}OH^-$ was measured to determine its contribution to the $^{17}O^-$ signal. The estimated $^{16}OH^-$ contribution to $^{17}O^-$ was always less than 0.03‰. Following oxygen isotope analyses, SEM images were taken of all analysis pits to ensure there was no overlap of pits, that the material analyzed in each were from a single mineral phase, and that they did not intersect cracks or inclusions. Measured $^{18}O/^{16}O$ and $^{17}O/^{16}O$ ratios are reported relative to VSMOW. San Carlos olivine ($\delta^{18}O = 5.32$; Kita et al., 2010) was measured regularly throughout the session to correct for instrumental mass bias. The external reproducibility (2SD) for $\delta^{18}O$, $\delta^{17}O$ and $\Delta^{17}O$ is 0.22, 0.50 and 0.53‰, respectively. As was also done for the magnesium isotope analyses conducted via SIMS, matrix effects for melilite and pyroxene were corrected by establishing correction schemes using mineral and glass standards (Tenner et al., 2013; Ushikubo et al., 2016).

3. Results

3.1. Petrology, mineralogy, and mineral chemistry

3.1.1. Petrology and mineralogy

CMS-1 is a coarse-grained inclusion that is approximately 3 × 5 mm in overall maximum dimensions. As viewed on the original cut slab surface (Fig. 1; Suppl. Figs. S1-S5), it is irregular in shape with an apparently undulating surface that gives the appearance of "cavities" filled with meteorite matrix and accretionary rim material. Figures 2-8 and Supplementary Figure S6a show X-ray maps and BSE images obtained on a thin section that was made perpendicular to the sawed

surface of the cut slab (see Suppl. Figs. S4-5). The thin section shows one relatively large area (the main mass of CMS-1, shown in the upper-left of Figure 2a; portions of this main mass are shown in Areas 1 and 2 of Fig. 2b) and a few smaller isolated areas (Areas 3-5 in Fig. 2b). These isolated areas are linked to the main mass of CMS-1 by a thick accretionary rim that encloses all and the isotopic signatures (discussed below) that they share in common. The apparent isolation of these areas from the main mass is most likely a manifestation in the thin section of the irregular shape of CMS-1. The areas outlined with white, numbered boxes (Fig. 2b and Suppl. Fig. 6a) correspond to regions in which major element concentrations, REE abundances, and isotopic compositions were determined (see Suppl. Tables 1-3).

CMS-1 is primarily composed of melilite, Ti-Al-rich pyroxene, and spinel with minor amounts of hibonite and perovskite. Melilite occurs as three distinct petrographic types (blocky with spinel inclusions, blocky without spinel inclusions, and lath-shaped with spinel inclusions). Throughout most of CMS-1 and the isolated areas, the melilite is blocky and anhedral in shape. The blocky melilite containing spinel inclusions is typically located adjacent to the blocky melilite devoid of spinel inclusions (Figs. 3-4). The lath-shaped melilite with spinel inclusions is located in Area 1; it is oriented perpendicular to the inclusion margin and projects radially inward (Fig. 3b). Figure 6 highlights (in yellow) the distribution of Ti-Al-rich pyroxene in CMS-1. This Ti-Al-rich pyroxene also occurs as three distinct petrographic types (blocky with spinel inclusions, blocky without spinel inclusions, and lath-shaped with spinel inclusions). Throughout much of CMS-1, Ti-Al-rich pyroxene is blocky and devoid of spinel inclusions (Figs. 4-5). However, Area 1 contains blocky pyroxene (on lower-right) and lath-shaped pyroxene (in between the lath-shaped melilite), both of which contain spinel inclusions (Fig. 3). Spinel is poikilitically enclosed by both

Ti-Al-rich pyroxene and melilite, but also occurs as larger grains intergrown with hibonite that form a mantle around the margin of the inclusion. Near the top of Figure 4 is a rounded nodule (shown enlarged in Fig. 8) that contains hibonite, a phase that is only present along the margin of the inclusion and otherwise absent from the interior of CMS-1. The accretionary rim that surrounds CMS-1 ranges up to 0.5 mm in thickness and contains abundant Ca-Fe silicates (andradite and iron-rich clinopyroxene) plus sodalite (Fig. 7). The ubiquitous presence of sodium-bearing feldspathoids in this accretionary rim is highlighted (in blue) in Figure 6.

3.1.2. Major element mineral chemistry

Table 1 shows the end-member major and minor element compositions for the primary phases in CMS-1 (melilite, pyroxene and spinel) in Areas 1-5 (major element data for individual spot analyses of melilite, Ti-Al-rich pyroxene, and spinel are listed in Suppl. Tables 1-3). Melilite compositions from the different petrographic types are shown in Figure 9. Lath-shaped melilite crystals in Area 1 are the most aluminous melilite, with a median value of $Åk_{28}$ but with a core composition that reaches $Åk_{18}$. Blocky melilite that contain spinel inclusions display a relatively restricted range in the Åk contents from $Åk_{27}$ to $Åk_{40}$, with a median value of $Åk_{33}$. Blocky melilite devoid of spinel inclusions displays the least aluminous compositions (median Åk contents of 40) but also shows the largest compositional variability.

Figure 10 displays the chemistry associated with the three petrographic types of pyroxenes. Most pyroxenes display a positive correlation between Al_2O_3 and TiO_2 (calculated assuming all Ti is Ti^{4+}) indicative of coupled substitution between aluminum and titanium. However, some pyroxenes (such as the lath-shaped as well as a few blocky pyroxenes in Area 1) display a negative

correlation that can result if the dominant coupled aluminum substitution is $2Al \Leftrightarrow 1Si$. Such a trend (illustrated in Fig. 10) may be indicative of the formation of kushiroite (formerly known as Ca-Tschermaks molecule; CaTs) (Kimura et al., 2009). Figure 11 shows the pyroxene compositions in terms of total titanium cations (per 6 oxygens) versus total cations (per 6 oxygens), where the structural formulae are calculated with all titanium as tetravalent. The dashed diagonal lines in Figure 11 demark constant ratios of $Ti^{3+}/(Ti^{3+} + Ti^{4+})$. Most of the data cluster around ~40% Ti^{3+}, with some as high as 75%. The lath-shaped pyroxenes from Area 1 overlap the main cluster at 40%, but extend down to less than 20% at the lowest total titanium contents. The analyses at the very bottom of the trend for Area 1 pyroxenes contain no detectable titanium in the trivalent state.

Spinel located in the interior of CMS-1 (whether as inclusions in pyroxene or melilite) is dominantly $MgAl_2O_4$. Spinel located near or within the margins of the inclusion displays elevated Fe content (up to ~16 wt.% FeO; Fig. 12a); the iron correlates linearly and negatively with magnesium, as expected for a solid solution between spinel and hercynite (Fig. 12b).

Table 2 reports the bulk composition of CMS-1 determined using energy dispersive spectroscopy (EDS) mapping of the thin section (including the relatively large area and the smaller isolated areas of the inclusion, but excluding the accretionary rim and matrix). Table 2 also presents estimates of the mineral modes ("mineral weight fractions") based on the bulk composition of CMS-1 and the average compositions of the primary phases (calculated from the range of compositions shown in Table 1). The mineral modes were calculated to best match the bulk composition using a constrained non-linear least-squares fit to minimize the residuals (SOLVER in MS-Excel).

3.1.3. Rare earth and other trace element abundances

Melilite and pyroxene are the predominant REE-bearing minerals in CMS-1. The REE abundances for several melilite and Ti-Al-rich pyroxene grains analyzed by SIMS are listed in Table 3 and plotted in Figure 13a (top panel). The Ti-Al-rich pyroxene has an LREE-depleted pattern (La~7–17 × CI; $[La/Sm]_{CI}$~0.4–0.6), with a large negative Eu anomaly (Eu/Eu*~0.1) and a HREE pattern that is relatively unfractionated (~40–70 × CI). The lath-shaped pyroxene plots towards the higher end of the range of REE concentrations (with the blocky pyroxene without spinel having the highest REE concentrations), while blocky pyroxene devoid of spinel plot towards the lower end of this range. Melilite shows a relatively flat LREE pattern (~6–19 × CI) and a positive Eu anomaly (Eu/Eu*~3) and depletion in the HREE ($[Gd/Lu]_{CI}$ = 5–7). The lath-shaped melilite displays the highest REE abundances in this mineral; the blocky melilite, with and without spinel inclusions has relatively lower REE concentrations. Figure 13b (bottom) shows the REE abundances estimated for the bulk composition of the CMS-1 inclusion based on the REE concentrations measured in the major REE-bearing minerals (melilite and pyroxene) and the modal abundances (mineral weight fractions) presented in Table 2. This calculated bulk REE pattern is relatively flat (i.e., a Group V pattern; Taylor and Mason, 1978), and is enriched in the REE by a factor of ~10 relative to CI chondrites (Palme and Beer, 1993). Pyroxene is the major host of thorium (Th = 0.08–0.78 ppm) whereas melilite contains very low abundances of this element (Th ≤ 0.07 ppm). Neither pyroxene nor melilite contained detectable amounts of uranium.

3.2. The isotopic compositions of Allende Fun CAI CMS-1

3.2.1. Magnesium and silicon isotopic compositions of CMS-1

294 The magnesium and silicon isotopic compositions of CMS-1, as determined by LA-MC-ICPMS
295 (Table 4), define relatively restricted ranges (δ^{25}Mg = 31.05–35.00‰, δ^{29}Si = 14.98–16.65‰)
296 (Figs. 14 and 15a). These values likely reflect mixtures of the three predominant phases (melilite,
297 pyroxene and spinel) given the relatively large volumes sampled by the laser spots (~40 μm in
298 diameter by ~40 μm in depth). Therefore, the averages of these values are likely to be a good
299 approximation of the bulk magnesium and silicon isotopic compositions of CMS-1. In this context,
300 the weighted averages of the δ^{25}Mg and δ^{29}Si values for CMS-1 are 15.54 ± 0.27‰ and 32.7 ±
301 0.5‰, respectively (where the errors reflect 95% confidence intervals).
302
303 The magnesium isotopic compositions of individual phases were also determined by SIMS and
304 these data are given in Table 5 and illustrated in Figure 15b,c. The magnesium isotopic
305 composition of individual melilite grains varies between 30.71 and 36.60‰ amu^{-1}, while that of
306 pyroxene ranges from 32.75 to 35.20‰ amu^{-1}. With regard to the different petrographic types,
307 lath-shaped melilite and blocky melilite without spinel are characterized by a similar median
308 magnesium isotope composition (33.1‰ amu^{-1}); blocky melilite with spinel displays a slightly
309 lower median value (31.5‰ amu^{-1}) (Fig. 15b). Similar systematics are observed for the different
310 petrographic types of pyroxene (Fig. 15c). However, there is considerable overlap between the
311 magnesium isotopic compositions of the different petrographic types of melilite and pyroxene. We
312 note that we have three or fewer analyses for some types (e.g., lath-shaped melilite and pyroxene),
313 which makes it challenging to make a statistically robust distinction between the magnesium
314 isotopic compositions of the different petrographic types. Spinel grains in the interior of the
315 inclusion typically exhibit magnesium isotopic compositions identical to the phases enclosing
316 them (either melilite or pyroxene) (Fig. 15b,c). For example, the magnesium isotopic composition

317 of spinel enclosed by melilite varies between 30.98 and 33.75‰ amu^{-1} (with spinel enclosed by
318 blocky melilite characterized by a slightly lower magnesium isotopic composition), while that of
319 spinel enclosed by pyroxene ranges from 33.63 to 37.48‰ amu^{-1}. The FeO-rich spinel located in
320 the rim displays the heaviest magnesium isotopic compositions, with values great than 38‰ amu^{-1}.
321 However, we cannot rule out potential matrix effects associated with the magnesium isotope
322 analysis of Fe-rich spinel because no Fe-rich spinel standard was analyzed during this analytical
323 session.
324
325 *3.2.2. ^{26}Al-^{26}Mg isotope systematics of CMS-1*
326 The $^{27}Al/^{24}Mg$ ratios determined by LA-MC-ICPMS span a limited range (2.9 – 5.4) and are
327 positively correlated with $\delta^{26}Mg^*$ values (Table 4) resulting in an initial $^{26}Al/^{27}Al$ ratio of (2.0±0.8)
328 $\times 10^{-5}$ (MSWD = 6.0) and an intercept ($\delta^{26}Mg_0$) of -0.8±0.2‰ (Fig. 16a). The SIMS data (Table
329 5) show that the $^{27}Al/^{24}Mg$ ratios of melilite, pyroxene and spinel span the range from 1.9 to 10.6
330 (melilite = 2.7–10.6; pyroxene = 1.9–6.3; spinel = 2.6–3.1) (Fig. 16). Regressing all the SIMS data
331 together results in a slope that is unresolved from zero ($^{26}Al/^{27}Al = -1.26±4.90 \times 10^{-6}$) and $\delta^{26}Mg_0$
332 = -0.11±0.12‰ (MSWD = 1.9), although a weak positive correlation exists for melilite with the
333 highest $^{27}Al/^{24}Mg$ ratios (i.e., $^{27}Al/^{24}Mg > 4.0$). Blocky melilite with spinel inclusions yields an
334 initial $^{26}Al/^{27}Al$ ratio of (-0.25±1.6) $\times 10^{-5}$ (MSWD = 0.14) and $\delta^{26}Mg_0$ of 0.09±0.47‰, while
335 blocky melilite without spinel displays an initial $^{26}Al/^{27}Al$ ratio of (1.97±2.0) $\times 10^{-5}$ (MSWD =
336 0.54) and $\delta^{26}Mg_0$ of -1.08±0.79‰ and lath-shaped melilite is characterized by an initial $^{26}Al/^{27}Al$
337 ratio of (0.24±1.3) $\times 10^{-5}$ (MSWD = 0.39) and $\delta^{26}Mg_0$ of 0.11±0.72‰ (Fig. 16b). Blocky pyroxene
338 with spinel inclusions is characterized by an initial $^{26}Al/^{27}Al$ ratio of (1.1±1.4) $\times 10^{-5}$ (MSWD =

0.17) and $\delta^{26}Mg_0$ of -0.40±0.35‰, whereas blocky pyroxene without spinel displays an initial $^{26}Al/^{27}Al$ ratio of (0.69±2.1) × 10^{-5} (MSWD = 1.11) and $\delta^{26}Mg_0$ of -0.01±0.38‰.

3.2.3. Oxygen isotopic composition of CMS-1

Table 6 and Figure 17 show the oxygen isotopic compositions of the primary phases (i.e., spinel, melilite, Ti-Al-rich pyroxene). The oxygen isotope data for spinel are relatively ^{16}O-enriched and define a slope of ~0.5 characteristic of mass-dependent fractionation. Some of the spinel enclosed by blocky melilite have relatively primitive compositions, i.e., close to the point where the spinel mass-dependent fractionation line intersects the CCAM line at the ^{16}O-rich end (point A in Fig. 17 with $\delta^{17}O$ and $\delta^{18}O$ ~ –49‰). Other spinel grains (especially those enclosed by pyroxene) are highly fractionated and plot close to where the spinel mass-dependent fractionation line intersects the mixing line defined by pyroxene (point B in Fig. 17, with $\delta^{17}O$ ~ –31.3‰ and $\delta^{18}O$ ~ –14.5‰). Pyroxene data plot exclusively on a mixing line and display a large range in isotopic composition ($\Delta^{17}O$ = –12.5 to –24.0‰); blocky pyroxene with spinel inclusions plot closer to the ^{16}O-rich end while pyroxene without spinel lies further towards the ^{16}O-poor end. Melilite is ^{16}O-poor, isotopically homogeneous, and plots near the intersection of the mixing line defined by the pyroxene data with the CCAM line (point C in Fig. 17), but below the terrestrial mass-dependent fraction line ($\Delta^{17}O$ = –4.9 to –2.8‰).

4. Discussion

4.1. Bulk composition of CMS-1 compared to condensation calculations

The heterogeneous textures and isotopic compositions observed in CMS-1 reflect either multiple reprocessing episodes of a single precursor or an aggregation of distinct, variably processed

362 precursor materials. With regards to the former, Grossman (2008a) showed that the bulk
363 compositions of CAIs, when corrected for evaporative loss of the moderately volatile elements,
364 are usually consistent with the chemical compositions of condensates predicted by equilibrium
365 thermodynamic calculations. In order to explain the range of pre-evaporation compositions, it was
366 suggested that CAIs must have condensed from nebular regions differing in total pressure from
367 10^{-6} to 10^{-3} bar (Grossman, 2008a), which is consistent with the range of pressures (and
368 temperatures) predicted by models of the protoplanetary disk during CAI formation (e.g., Charnoz
369 et al., 2011; Ciesla, 2010; D'Alessio et al., 1998; Dubrulle et al., 1995; Lesniak and Desch, 2011).
370 The present-day bulk composition of CMS-1 (shown in Table 2) is similar to that of compact Type
371 A and Type B CAIs. When plotted in MgO-SiO_2 space (Fig. 18), this bulk composition falls along
372 the predicted condensation path for gas of solar composition at a total pressure of 10^{-3} to 10^{-6} bar
373 (Grossman et al., 2008a). The calculations of Grossman et al. (2008a) predict equilibrium
374 condensates at these pressures, and in this region of MgO-SiO_2 space, to be represented by an
375 assemblage of melilite-spinel-diopside, which is similar to the observed mineralogy of CMS-1.
376 However, the distinct textures and associated large mass-dependent fractionations observed in Mg,
377 Si and O isotopes indicate that CMS-1 experienced one or more melting events along with
378 extensive evaporative loss, that may have resulted in significant changes to its bulk chemical
379 composition (see sections 4.3. below). If true, the present-day bulk composition of CMS-1 must
380 be corrected for evaporation of the moderately volatile elements (e.g., magnesium and silicon). If
381 CMS-1 represents an aggregation of distinct, variably processed precursor materials, these
382 materials all still experienced large degrees of mass-dependent fractionation associated with
383 evaporative loss. As such, their present-day compositions still need to be corrected for this to infer
384 the original compositions of the precursors.

385

386 The REE distributions in melilite and Ti-Al-rich pyroxene are indicative of fractional
387 crystallization from a melt (Beckett et al., 1990; Simon et al., 1991; Davis et al., 1996; Lundstrom
388 et al., 2006) independent of their crystal habit or petrographic type (Fig. 13a). The large
389 complimentary Eu anomalies observed in both phases are consistent with melilite reaching the
390 liquidus prior to onset of pyroxene crystallization (Stolper and Paque, 1986). Spinel does not
391 incorporate appreciable amounts of the REE; therefore, the concentrations of REE in melilite and
392 pyroxene, along with their modal abundances (and a dilution factor set by the modal volume of
393 spinel), can be used to estimate the bulk REE composition of CMS-1. The bulk REE pattern
394 calculated for CMS-1 is relatively flat and the REE concentrations are enriched ~10 times relative
395 to CI chondrites. This suggests that the CMS-1 precursor material(s) condensed from the solar
396 nebula with chondritic relative REE abundances and that the REE were not significantly
397 fractionated during the thermal event(s) that produced the large mass-dependent fractionations of
398 magnesium, silicon and oxygen observed in CMS-1. There appear to be no anomalies in Eu or Yb,
399 which indicates that volatility-controlled events under the canonical solar nebular condition
400 (Hiyagon et al., 2011) were not responsible for the bulk REE pattern. This suggests that this REE
401 pattern was established during the original condensation of CMS-1 precursor material(s) and was
402 not modified significantly during subsequent melting events.
403

404 CMS-1 is also enriched in thorium relative to chondritic composition (upwards of 30 × CI), but
405 highly depleted in uranium, similar to other FUN CAIs (Chen and Wasserburg, 1981; Holst et al.,
406 2013). This is unlike most CAIs that typically display Th/U ratios of ~3-4 (Brearley and Jones,
407 1998). Alteration veins that crosscut CMS-1 contain no measureable amounts of uranium (given

408 the detection limits); therefore if aqueous alteration is responsible for the observed depletion of
409 uranium in the inclusion, it has been completely removed from the system. Alternatively, uranium
410 may have been depleted during the high degree of melt evaporation experienced by CMS-1, but
411 this remains to be more rigorously evaluated.
412
413 *4.2. Oxygen fugacity associated with melting events involved in CMS-1 formation*
414 The oxygen fugacity of the gas in equilibrium with the melt from which CMS-1 crystallized can
415 be estimated employing the method outlined by Grossman et al. (2008b) using the following
416 equations:
417
418 $\ln K'_1 = 4\ln[X_{T3P}/X_{T4P}X_{Di}] - 4\ln \gamma_{Di} + 2\ln X_{Åk} + \ln f_{O2}$ (1)
419
420 and
421
422 $\ln K'_3 = 4\ln[X_{T3P}/X_{T4P}] - 2\ln[X_{CaTs}X_{Di}] - 2\ln[\gamma_{CaTs}\gamma_{Di}] + 2\ln X_{Ge} + \ln f_{O2}$ (2)
423
424 where X_{T3P}, X_{T4P}, X_{Di}, X_{CaTs}, $X_{Åk}$, X_{Ge} are the mole fractions of the pyroxene and melilite
425 components and γ_{CaTs}, and γ_{Di} are activities of pyroxene components; the values of $\ln K'_1$ and
426 $\ln K'_3$ are reported by Grossman et al. (2008b) for a temperature of 1509 K. For the purposes of
427 this estimation, we assume that the most primitive pyroxene (i.e., with the highest TiO_2 content
428 shown in Table 1) is the best candidate to represent an equilibrium assemblage with the most
429 åkermanitic melilite (since melilite is predicted to begin crystallization prior to pyroxene).
430 Inserting this compositional information into equations 1 and 2 results in limited estimates for the

431 f_{O_2} of the gas in equilibrium with the melt, ranging from log f_{O_2} of -19.7 to -19.1 (assuming a
432 temperature of 1509 K). These estimates are broadly consistent with melting of CMS-1 precursor
433 material(s) under nebular conditions at temperatures of 1500 to 1700 K (Grossman et al., 2008b
434 and references therein). We note, however, that the solidus and the liquidus of forsterite-rich
435 precursor(s) to CMS-1 are likely to be ~1573 and 1800 K, respectively (see Mendybaev et al.,
436 2016).
437
438 *4.3. Implications of the magnesium and silicon isotope compositions of CMS-1*
439 The bulk composition of CMS-1 is typical of compact Type A and Type B CAIs and an equivalent
440 melt would have the predicted crystallization sequence spinel –> melilite –> pyroxene, which is
441 consistent with the mineralogy and oxygen isotopic composition (see following section) of this
442 inclusion. The earliest-crystallizing melilite is characterized by a magnesium isotopic fractionation
443 in excess of 30‰ amu^{-1}. This observation implies that CMS-1 or its precursor components had
444 already undergone a large degree of mass-dependent fractionation, and thereby lost the majority
445 of its moderately refractory elements through evaporation prior to the onset of fractional
446 crystallization.
447
448 That the magnesium isotopic compositions of spinel in the interior of CMS-1 are similar to their
449 host phases indicates that the magnesium isotopic composition of interior spinel continued to re-
450 equilibrate with the surrounding melt until poikilitically enclosed by either melilite or pyroxene.
451 The FeO-rich spinel in the rim of CMS-1 displays the largest degree of mass-dependent
452 fractionation (assuming it is not due to potential matrix effects), suggesting this spinel either
453 maintained equilibrium with the continually evolving melt until complete crystallization of the

454 inclusion occurred or it was forming while the final melt was undergoing an additional evaporation
455 event. Nevertheless, these data indicate that mass-dependent fractionation of magnesium likely
456 continued throughout the crystallization sequence of CMS-1.
457
458 We can employ the relationship between the loss of elemental magnesium and silicon and the
459 extent of magnesium and silicon isotopic fractionation in the evaporation residues to estimate the
460 precursor composition, using its measured magnesium and silicon isotopic compositions. The
461 experimentally determined kinetic fractionation factors of magnesium, silicon and oxygen isotopes
462 during evaporation of forsterite-rich melts (reported in the companion paper by Mendybaev et al.,
463 2016) and the measured mass-dependent fractionation of silicon and magnesium reported here for
464 CMS-1 suggest that ~80% of silicon and ~85% magnesium were lost from its precursor material
465 through evaporative processes. Adding back the silicon and magnesium believed lost to
466 evaporation to our estimate of the current bulk composition of CMS-1 results in a precursor
467 composition close to that expected to condense from a gas of solar composition (Fig. 18; see also
468 Fig. 11 of Mendybaev et al., 2016). The general magnitude of loss estimated here is independent
469 of whether the current composition of CMS-1 represents the thermal processing of a single
470 precursor material multiple times or thermal processing of multiple, distinct precursor materials
471 that later aggregated to form CMS-1 as all phases display large degrees of mass-dependent
472 fractionation.
473
474 *4.4. Implications of the oxygen isotope systematics of CMS-1*
475 The oxygen isotopic composition of CMS-1 suggests a formation history that involved at least
476 three stages of evolution. These three stages could be applied to two different formation scenarios

with respect to CMS-1: either thermal processing of a single precursor material multiple times or thermal processing of multiple distinct precursor materials that later aggregated to form CMS-1. The first stage involved the initial melting of the precursor condensate material(s) to produce the parental melt. The initial oxygen isotopic composition of this parental melt is best constrained by the first phase to crystallize (i.e., spinel), where the most primitive spinel identified from CMS-1 is characterized by a ^{16}O-rich oxygen isotopic composition, suggesting that the oxygen isotopic composition of the parental melt originated near the intersection of the mass-dependent fractionation line defined by the spinel data with the CCAM line (point A in Fig. 17 with δ^{17}O and δ^{18}O ~-49‰). Subsequent to this initial melting event, the second stage involved evaporation during progressive crystallization of the spinel. This stage resulted in the mass-dependent fractionation of oxygen (and silicon and magnesium; see below) in the melt as the spinel crystallized in equilibrium with it. This mass-dependent fractionation line is similar to that characterized by refractory phases measured in other FUN CAIs (Clayton and Mayeda, 1977; Lee et al., 1980; Clayton et al., 1984; Davis et al., 1991; Makide et al., 2009; Thrane et al., 2008; Krot et al., 2014) and in residues produced by evaporation of forsteritic melts in vacuum (see Fig. 10 of Mendybaev et al., 2016).

This event involving evaporation of the chemically evolving melt also resulted in the mass-dependent fractionation of melilite and pyroxene that crystallized following the spinel. As such, the oxygen isotopic composition of the melilite would lie along the mass-dependent fractionation line defined by the spinel, while pyroxene, as the last phase to crystallize from the melt, would be located at the most fractionated end of the mass-dependent fractionation line (i.e., the "bend" in the array observed in Fig. 17 at δ^{17}O ~ –31.3‰ and δ^{18}O ~ –14.5‰, point B). The full range of

oxygen isotope fractionation observed in the least fractionated spinel and the pyroxene (27.4‰ in $\delta^{18}O$) is consistent with predicted values based on the mass-dependent fractionation of magnesium and silicon isotopes (Davis et al., 1990; Mendybaev et al., 2013b, 2016; Wang et al., 2001).

The final stage in the evolution of the oxygen isotope systematics requires exchange and equilibration between the ^{16}O-rich reservoir in which CMS-1 experienced the two earlier stages and a ^{16}O-poor reservoir. This is inferred from the linear array defined by the pyroxene data and the clustering of melilite at the ^{16}O-poor end of this array (point C in Fig. 17). The tight clustering of melilite does not allow extrapolation back to the mass-dependent fractionation line defined by the spinel, thereby hindering the ability to determine whether melilite crystallized from a still-evolving melt due to evaporation, or if evaporation had ceased prior to melilite crystallization. It is also unclear under what conditions exchange between ^{16}O-rich and ^{16}O-poor reservoirs occurred. Several studies have proposed that CAIs condensed in ^{16}O-rich regions of the inner nebula and were then transported into regions where back-reaction of solids with ^{16}O-poor gas could occur (Clayton et al., 1977; Clayton, 1993; Yurimoto et al., 1998; Aléon et al., 2002, 2005; Fagan et al., 2004; Krot et al., 2004) or vice versa (Kawasaki et al., 2012; Aléon, 2016). However, given the extensive history of thermal metamorphism and alteration of the Allende parent body (Scott et al., 1992; Krot et al., 1998), and thereby CMS-1, it is difficult to distinguish the process(es) responsible for producing the observed mixing lines, which could be due to nebular exchange or parent body alteration (Wasson et al., 2001; Imai and Yurimoto, 2003; Fagan et al., 2004; Krot et al., 2004).

4.5. Implications for the presence of live ^{26}Al during formation of CMS-1

522 Several features emerge from the ^{26}Al-^{26}Mg isotope systematics of CMS-1 determined via LA-
523 MC-ICPMS (Table 4) and SIMS (Table 5) that relate to its formation environment and subsequent
524 thermal history. The foremost of these is that the LA-MC-ICPMS data appear to define a positive
525 correlation in the ^{26}Al-^{26}Mg isochron plot (Fig. 16a) that suggests the former presence of live ^{26}Al.
526 Specifically, these data would suggest an initial $^{26}Al/^{27}Al$ ratio of $(2.0\pm0.8) \times 10^{-5}$, with an a $\delta^{26}Mg_0$
527 of -0.8±0.2‰ at the time of last equilibration of the ^{26}Al-^{26}Mg system in CMS-1. However, as
528 evident from the value of the Mean Squared Weighted Deviation (i.e., MSWD = 6.0), the scatter
529 in these data exceeds that predicted by analytical uncertainties, indicating this is not a statistically
530 robust correlation. This apparent scatter could reflect the incorporation of isotopically distinct
531 precursor material(s) that were not fully equilibrated during the melting and formation of CMS-1
532 or could be due to varying degrees of post-crystallization equilibration in different phases of CMS-
533 1. Either of these two scenarios would also be consistent with the SIMS data (discussed below)
534 that display apparent trends with varying slopes and initial $^{26}Mg/^{24}Mg$ ratios ($\delta^{26}Mg_0$) depending
535 on the habit of the host phase.
536
537 We note that none of the trends defined by the SIMS data (Fig. 16b,c) define a slope that is
538 statistically resolved from zero; however, these regressions provide a qualitative indication of the
539 possible presence of live ^{26}Al in the precursor material(s) for CMS-1 and its subsequent evolution.
540 In particular, the SIMS ^{26}Al-^{26}Mg data for the blocky melilite without spinel inclusions show a
541 hint of a correlation line that defines a slope corresponding to an initial $^{26}Al/^{27}Al$ ratio of (1.97±2.0)
542 $\times 10^{-5}$ (MSWD = 0.54) and $\delta^{26}Mg_0$ of -1.1±0.8‰ (Fig. 16b). Although not statistically resolved
543 from a slope of zero ($^{26}Al/^{27}Al \leq 4.0\times10^{-5}$), this regression is consistent in terms of the initial
544 $^{26}Al/^{27}Al$ ratio and the $\delta^{26}Mg_0$ value with the regression based on the LA-MC-ICPMS data. It

provides an indication of ^{26}Al being present during the formation of CMS-1 or its precursor components. The well-resolved negative $\delta^{26}Mg_0$ value inferred from the LA-MC-ICMPS data for CMS-1 as well as the SIMS data for the blocky melilite without spinel suggests that at least one of the CMS-1 precursors formed in a nebular environment characterized by an initial magnesium isotope composition distinct from that of normal as well as other FUN CAIs (e.g., Krot et al., 2012). This is further evidence for the existence of heterogeneity in the initial $^{26}Mg/^{24}Mg$ ratio ($\delta^{26}Mg_0$) of the early solar system (Wasserburg et al., 2012). Data for blocky melilite with spinel inclusions and lath-shaped melilite define upper limits on the initial $^{26}Al/^{27}Al$ ratio ($\leq 1.3\times10^{-5}$ and $\leq 1.5\times10^{-5}$, respectively) that are lower than that defined by the blocky melilite without spinel, as well as $\delta^{26}Mg_0$ values (0.1±0.5‰ and 0.1±0.7‰) that cannot be resolved from the terrestrial value. On the other hand, blocky pyroxene with spinel has an initial $^{26}Al/^{27}Al$ ratio $\leq 2.5\times10^{-5}$ and a $\delta^{26}Mg_0$ (-0.40±0.35‰) that is resolvably negative. Blocky pyroxene without spinel has an initial $^{26}Al/^{27}Al$ ratio $\leq 2.8\times10^{-5}$ and a $\delta^{26}Mg_0$ (0.0±0.4‰) that is indistinguishable from the terrestrial value.

The apparent differences in the ^{26}Al-^{26}Mg isotope systematics between different phases and petrographic settings (characterized by different habits) could be indicative of two possible scenarios. First, each mineral and its habit could represent distinct precursor materials that were thermally processed but not fully equilibrated during the melting and formation of CMS-1. If true, this scenario would indicate that the early solar system was isotopically heterogeneous in both ^{26}Al and its magnesium isotopic composition at the time of formation of CMS-1. Alternatively, a single precursor material could have aggregated and then undergone multiple heating events that resulted in melting of this precursor as well as post-formation thermal equilibration of CMS-1. In this case, the ^{26}Al-^{26}Mg system in different phases and distinct petrographic settings could have been

affected to varying degrees by partial melting (due to differences in the refractoriness of the phase) or post-crystallization thermal equilibration (due to differences in magnesium diffusivity in distinct phases with different compositions and crystal habits; e.g., Morioka and Nagasawa, 1991; Liermann and Ganguly, 2002; Cherniak, 2010; Müller et al., 2013).

The values for the initial $^{26}Al/^{27}Al$ ratio and $\delta^{26}Mg_0$ inferred from previously studied FUN CAIs are quite variable, although the initial $^{26}Al/^{27}Al$ ratio is typically significantly lower than the canonical value of $\sim 5\times10^{-5}$ (e.g., Fig. 24 of Krot et al., 2012). Previous investigations have suggested several possibilities for their lower initial $^{26}Al/^{27}Al$ ratios (Krot et al., 2012; and references therein): 1) early formation, prior to the injection and homogenization of ^{26}Al in the solar nebula; 2) late formation (after normal CAIs) following the decay of much of the initial inventory of ^{26}Al; 3) contemporaneous formation with normal CAIs, but in a region with much lower ^{26}Al abundances than in normal CAIs (i.e., spatial heterogeneity in the distribution of ^{26}Al in the early solar system); 4) preferential loss (likely due to volatilization) of the ^{26}Al carrier from their precursor materials; and 5) formation in an extrasolar environment having a lower than canonical ^{26}Al abundance. Holst et al. (2013) showed recently that the initial $^{182}Hf/^{180}Hf$ ratio in a FUN CAI was similar to that in normal CAIs, and suggested that these objects were likely formed contemporaneously in regions of the solar nebula characterized by grossly different initial ^{26}Al abundances. However, since there are no absolute chronological constraints as yet for FUN CAIs, we cannot rule out any of the previously discussed possibilities with certainty.

4.6. Implications for the formation of CMS-1 and thermal-chemical evolution of the early Solar System

591 The chemical and isotopic compositions of normal and FUN CAIs suggest that although the
592 precursors of these refractory materials condensed in similar environments, they subsequently
593 evolved under vastly different conditions (e.g., Katayama et al., 2012; Kawasaki et al., 2012; Aléon
594 2016). The dynamics of protoplanetary disks generate an enormous range of physical and chemical
595 conditions. Gradients in gas pressure, dust density and temperature are thought to characterize
596 protoplanetary disks as a function of radial distance from the Sun, vertical position relative to the
597 disk midplane, and time as the disk evolves from an active to passive state. The gas density
598 distribution ρ(r,z) can be obtained by integrating:

599 $$\rho(r,z) = \frac{\Sigma(r)}{H(r)\sqrt{2\pi}} exp\left[-\frac{z^2}{2H(r)^2}\right] \quad (3)$$

600 where Σ(r) is the surface density at some heliocentric distance r, H(r) is the thickness of the disk,
601 and z is the vertical coordinate measured from the midplane. Equation 3 shows that the vertical
602 distribution of gas density will decrease by several orders of magnitude from the midplane towards
603 the outer edges of the disk (e.g., Dubrulle et al., 1995; D'Alessio et al., 1998; Ciesla, 2010; Charnoz
604 et al., 2011; Lesniak and Desch, 2011). Dust is transported vertically through turbulent diffusion
605 that is proportional to the gas density and a dust diffusion coefficient leading to large vertical
606 gradients in the dust density (Dubrulle et al., 1995; Ciesla, 2010; Charnoz et al., 2011). These
607 dynamics result in dust being exposed to different ambient gas pressures (Ciesla, 2010) as well as
608 size sorting of the dust due to gravitational settling (Dubrulle et al., 1995; Ciesla, 2010; Charnoz
609 et al., 2011). As such, the midplane is characterized by high gas pressures and high dust densities,
610 whereas the disk edges are characterized by low gas pressures and dust densities.
611
612 Determination of the temperature structure is a more complex problem. The primary heating
613 mechanisms for a disk are viscous dissipation and irradiation by the central star (e.g., D'Alessio et

614 al., 1998; Lesniak and Desch, 2011). Viscous heating is proportional to the mass accretion rate and
615 will decrease from the midplane to the edges of the disk through radiative transfer, which itself is
616 a function of the optical depth of the disk (e.g., surface density, dust-gas ratio, and the opacity of
617 the dust grains). Similarly, heating due to irradiation from the central star is proportional to the
618 luminosity of the central star and the angle of incidence; it decreases from the edge of the disk
619 towards the midplane as a function of its absorbance by dust (which depends on factors such as
620 dust density, the dust-gas ratio and the opacity of the dust grains). For a radius of circa 1-5 AU or
621 less, viscous dissipation is the main energy source for regions near the midplane (D'Alessio et al.,
622 1998; Lesniak and Desch, 2011) assuming an active disk. In these regions viscous heating may
623 lead to vertical temperature gradients on the order of a few hundred degrees or more (D'Alessio et
624 al., 1998; Lesniak and Desch, 2011); these gradients are still much smaller than those for gas and
625 dust densities. Specifically, the vertical temperature structure of the innermost disk depends
626 strongly on the mean optical depth and the angle of incidence of radiation from the central star.
627 Within 1-5 AU, irradiation may also produce a very thin, superheated surface layer due to the
628 relatively low angle of incidence of radiation from the star. For a radius greater than circa 1-5 AU,
629 irradiation from the central star becomes more significant and the vertical temperature profile may
630 become isothermal or produce a temperature inversion since the disk surface temperature may be
631 higher than the photosphere temperature (D'Alessio et al., 1998; Lesniak and Desch, 2011). As
632 such, the vertical temperature structure will change as a function of heliocentric distance and time.
633
634 Though the reprocessing and/or melting of CAI precursor materials is mostly like dominated by
635 discrete heating events (Richter et al., 2006), subsequent chemical and isotopic evolution of the
636 melt upon cooling would be controlled by ambient conditions of the disk. The midplane of the

protoplanetary disk should be characterized by high gas pressures and high dust densities, while at a given vertical height above the midplane, gas pressures and dust densities decrease. Processing material in regions of high dust densities at the midplane will also promote higher f_{O_2} conditions (e.g., during chondrule formation). The equations that govern the theory of evaporation (e.g., Richter et al., 2002, 2007; Young and Galy, 2004) show that, under the conditions that characterize the midplane, evaporation and isotopic fractionation will be limited (assuming ambient temperature gradients are negligible in comparison). In contrast, conditions believed to characterize the edges of the disk will promote evaporation and isotopic fractionation (Charnoz et al., 2011; Aléon, 2016). Since most material is confined to regions near the midplane due to gravitational settling, the resulting products of ambient or discrete heating events will display limited chemical and isotopic fractionation. This is consistent with the meteoritic observations (e.g., Grossman, 2008a) that show that variation in the magnesium, silicon and oxygen isotopic compositions of most CAIs (i.e., normal CAIs) is limited to a few permil amu^{-1}. Inclusions (such as FUN CAIs) that display mass-dependent fractionation of magnesium, silicon and oxygen up to several tens of per mil amu^{-1} may be the result of a small fraction of material being transported vertically to regions near the edges of the disk through turbulent diffusion where evaporation is promoted during heating events. This would result in a minor fraction of CAIs that display large degrees of chemical and isotopic fractionation. Extreme mass loss from precursor materials under these conditions is also possible, resulting in chemically and physically distinct products (perhaps forming HAL-like FUN CAIs; Fahey et al., 1987) and, in addition to physical sorting of material as discussed above, may aid in explaining the limited number of meteoritic samples observed to have undergone large degrees of evaporation.

5. Conclusions

The chemical and isotopic composition of normal and FUN CAIs suggests that these materials condensed in similar environments, but subsequently evolved under vastly different conditions. Detailed petrologic and isotopic analyses of the Allende FUN CAI CMS-1 indicate a complex multi-stage history of reprocessing following the initial melting of its precursor material. The CMS-1 precursor material formed in a ^{16}O-rich region of the inner solar nebula. Subsequent melting of the precursor material was accompanied by substantial surface evaporative loss of magnesium, silicon and oxygen. This evaporative loss resulted in a bulk composition similar to that of compact Type A and Type B CAIs, although the original condensate composition was far richer in MgO and (and to a lesser extent) SiO_2. Theoretical and experimental considerations indicate that the precursor material had a bulk composition consistent with condensation from a gas of solar composition, with an initial mineral assemblage similar to forsterite-bearing CAIs. Sorting of early solar system materials into distinct physical and chemical regimes, along with discrete heating events, could explain the chemical and isotopic differences between normal and FUN CAIs.

Acknowledgements:

We thank J.-D. Bodénan, A. El Goresy, an anonymous reviewer and S. S. Russell (AE) for comments and suggestions which improved this paper. This work was supported by the NASA Earth and Space Sciences Fellowship (award NNX12AN04H to C. D. Williams), NASA Origins of Solar Systems program (award NNX11AK56 to M. Wadhwa), NASA Cosmochemistry program (awards NNX11AD43G to G. J. MacPherson and MNX13AH09G to F. M. Richter), and NASA Emerging Worlds program (award NNX15AH68G to G. J. MacPherson). The ASU SIMS

683 lab acknowledges support from NSF EAR 1352996. This paper is dedicated to the memory of Ian
684 D. Hutcheon.

685 **References**

686 Aléon J., Krot, A. N. and McKeegan K. D. (2002) Calcium-aluminum-rich inclusions and
687 amoeboid olivine aggregates from the CR carbonaceous chondrites. *Meteorit. Planet. Sci* **37**,
688 1729–1755.

689 Aléon J. (2016) Oxygen isotopes in the early protoplanetary disk inferred from pyroxene in a
690 classical type B CAI. *Earth Planet. Sci. Lett.* **440**, 62-70.

691 Amelin Y., Krot A. N., Jutcheon I. D. and Ulyanov A. A. (2002) Lead isotopic ages of chondrules
692 and calcium-aluminum-rich inclusions. *Science* **297**, 1678-1683.

693 Beckett J. R., Spivack A. J., Hutcheon I. D., Wasserburg G. J. and Stolper E. M., (1990) Crystal
694 chemical effects on the partitioning of trace elements between mineral and melt; an
695 experimental study of melilite with applications to refractory inclusions from carbonaceous
696 chondrites. *Geochim. Cosmochim. Acta* **54**, 1755–1774.

697 Bouvier A., Wadhwa M., Bullock E. S. and MacPherson G. j. (2010) Pb-Pb dating of a CAI from
698 the reduced CV3 chondrite Vigarano. *73rd Annual Meteoritical Society Meeting*, #5400 (2010)
699 (abstract).

700 Brigham C. A. (1990) Isotopic heterogeneity in calcium-aluminum-rich meteoritic inclusions.
701 *PhD Thesis, CalTech*, 266 p.

702 Bullock E. S., MacPherson G. J., Nagashima K., Krot A. N., Petaev M. I., Jacobsen S. B. and
703 Ulyanov A. A. (2012) Forsterite-bearing type B refractory inclusions from CV3 chondrites:
704 from aggregates to volatilized melt droplets. *Meteorit. Planet. Sci.* **47**, 2128-2147.

705 Charnoz S., Fouchet L., Aléon J. and Moreira M. (2011) Three-dimensional Lagrangian turbulent
706 diffusion of dust grains in a protoplanetary disk: Method and first applications. *Astrophys. J.*
707 **737**, 514-529.

Cherniak D. J. and Dimanov A. (2010) Diffusion in pyroxene, mica and amphibole. *Rev. Mineral. Geochem.* **72**, 641-690.

Ciesla F. J. (2010) Residence times of particles in diffusive protoplanetary disk environemnts. I. Vertical motions. *Astrophys. J.* **723**, 514-529. p. 33 (17 pp.)

Clayton R. N. (1993) Oxygen isotopes in meteorites. *Annual Review of Earth and Planetary Sciences* **21,** 115–149.

Clayton R. N. and Mayeda T. K. (1977) Correlated oxygen and magnesium isotope anomalies in Allende inclusions, I: Oxygen. *Geophys. Res. Lett.* **4**, 295-298.

Clayton R. N., Mayeda T. K., and Epstein S. (1978) Isotopic fractionation of silicon in Allende inclusions. *Proc. Lunar Planet. Sci. Conf. 9th* pp. 1267-1278.

Clayton R. N., Onuma N., Grossman L. and Mayeda T. K. (1977) Distribution of the pre-solar component in Allende and other carbonaceous chondrites. *Earth Planet. Sci. Lett.* **34**, 209-224.

Clayton R. N., MacPherson G. J., Hutcheon I. D., Davis A. M., Grossman L., Mayeda T. K., Molini-Velsko C., Allen J. M. and El Goresy A. (1984) Two forsterite-bearing FUN inclusions in the Allende meteorite. *Geochim. Cosmochim. Acta* **48**, 535–548.

Conard R. (1976) A study of the chemical composition of Ca-Al-rich inclusions from the Allende meteorite. Thesis, Oregon State University, MS.

Connelly J. N., Bizzarro M., Krot A. N., Nordlund A., Wielandt D. and Ivanova M. A. (2012) The absolute chronology and thermal processing of solids in the solar protoplanetary disk. *Science* **338**, 651-655.

D'Alessio P., Cantó J., Calvet N. and Lizano S. (1998) Accretion disks around young objects. I. The detailed vertical structure. *Astrophys. J.* **500**, 411-427.

730 Davis A. M., Hashimoto A., Clayton R. N. and Mayeda T. K. (1990) Isotope mass fractionation
731 during evaporation of Mg_2SiO_4. *Nature* **347**, 655-658.
732 Davis A. M., MacPherson G. J., Clayton R. N., Mayeda T. K., Sylvester P. J., Grossman L., Hinton
733 R. W. and Laughlin J. R. (1991) Melt solidification and late-stage evaporation in the evolution
734 of a FUN inclusion from the Vigarano C3V chondrite. *Geochim. Cosmochim. Acta* **55**, 621–
735 637.
736 Davis A. M., Richter F. M., Simon S. B. and Grossman L. (1996) The effect of cooling rate on
737 melilite/liquid partition coefficients for Y and REE in Type B CAI melts. *Lunar Planet. Sci.*
738 *XXVII. Lunar Planet. Inst., Houston*, 291–292.
739 Davis A. M., Richter F. M., Mendybaev R. A., Janney P. E., Wadhwa M. and McKeegan K. D.
740 (2015) Isotopic mass fractionation laws for magnesium and their effects on ^{26}Al-^{26}Mg
741 systematics in solar system materials. *Geochim. Cosmochim. Acta* **158**, 245–261.
742 Dubrulle B., Morfill G. and Sterzik M. (1995) The dust subdisk in the protoplanetary nebula.
743 *Icarus* **114**, 237-246.
744 Fagan T. J., Krot A. N., Keil K., and Yurimoto H. (2004) Oxygen isotopic evolution of amoeboid
745 olivine aggregates in the reduced CV3 chondrites Efremovka, Vigarano, and Leoville.
746 *Geochim. Cosmochim. Acta* **68**, 2591–2611.
747 Fahey A. J., Goswami J. N., McKeegan K. D. and Zinner E. (1987) ^{26}Al, ^{244}Pu, ^{50}Ti, REE, and
748 trace element abundances in hibonite grains from CM and CV meteorites. *Geochim.*
749 *Cosmochim. Acta* **51**, 329-350.
750 Grossman L., Ebel D. S., Simon S. B., Davis A. M., Richter F. M. and Parsad N. M. (2000) Major
751 element chemical and isotopic compositions of refractory inclusions in C3 chondrites: the
752 separate roles of condensation and evaporation. *Geochim. Cosmochim. Acta* **64**, 2879-2894.

753 Grossman L., Simon S. B., Rai V. K., Thiemens M. H., Hutcheon I. D., Williams R. W., Galy A.,
754 Ding T., Fedkin A. V., Clayton R. N. and Mayeda T. K. (2008a) Primordial compositions of
755 refractory inclusions. *Geochim. Cosmochim. Acta* **72**, 3001–3021.
756 Grossman L., Beckett J. R., Fedkin A. V., Simon S. B. and Ciesla F. J. (2008b) Redox conditions
757 in the Solar Nebula: observational, experimental, and theoretical constraints. *Rev. Mineral.*
758 *Geochem.* **68**, 93-140.
759 Hashimoto A. (1990) Evaporation kinetics of forsterite and implications for the early solar nebula.
760 *Nature* **347**, 53–55.
761 Hiyagon H., Yamakawa A., Ushikubo T., Lin Y. and Kimura M. (2011) Fractionation of rare earth
762 elements in refractory inclusions from the Ningqiang meteorite: Origin of positive anomalies
763 in Ce, Eu, and Yb. *Geochim. Cosmochim. Acta* **75**, 3358-3384.
764 Holst J. C., Olsen M. B., Paton C., Nagashima K., Schiller M., Wielandt D., Larsen K. K., Connelly
765 J. N., Jørgensen J. K., Krot A. N., Nordlund Å. and Bizzarro M. (2013) ^{182}Hf-^{182}W age dating
766 of a ^{26}Al-poor inclusion and implications for the origin of short-lived radioisotopes in the early
767 solar system. *PNAS* **22**, 8819-8823.
768 Imai H. and Yurimoto H. (2003) Oxygen isotopic distribution in an amoeboid olivine aggregate
769 from the Allende CV chondrite: Primary and secondary processes. *Geochim. Cosmochim. Acta*
770 **67,** 765–772.
771 Jacobsen B., Yin Q.-Z., Moynier F., Amelin Y., Krot A. N., Nagashima K., Hutcheon I. D. and
772 Palme H. (2008) 26Al-26Mg and 207Pb-206Pb systematics of Allende CAIs: canonical solar
773 initial 26Al/27Al ratio reinstated. *Earth Planet. Sci. Lett.* **272**, 353-364.
774 Janney P. E., Richter F. M., Mendybaev R. A., Wadhwa M., Georg R. B., Watson E. B. and Hines
775 R. R. (2011) Matrix effects in the analysis of Mg and Si isotope ratios in natural and synthetic

776 glasses by laser ablation-multicollector ICPMS: a comparison of single- and double-focusing
777 mass spectrometers. *Chem. Geol.* **281**, 26–40.
778 Katayama J., Itoh S. and Yurimoto H. (2012) Oxygen isotopic zoning of reversely zoned melilite
779 crystals in a fluffy type A Ca-Al-rich inclusion from the Vigarano meteorite. *Meteorit. Planet.*
780 *Sci* **47**, 2094-2106.
781 Kawasaki N., Sakamoto N. and Yurimoto H. (2012) Oxygen isotopic and chemical zoning of
782 melilite crystals in a type A Ca-Al-rich inclusion of Efremovka CV3 chondrite. *Meteorit.*
783 *Planet. Sci* **47**, 2084-2093.
784 Kimura M., Mikouchi T., Suzuki A., Miyahara M., Ohtani E. and Goresy A. L. (2009) Kushiroite,
785 CaAlAlSiO6: a new mineral of the pyroxene group from the ALH 85085 CH chondrite, and
786 its genetic significance in refractory grains. *American Mineralogist* **94**, 1479-1482.
787 Kita N. T., Ushikubo T., Fu B. and Valley J. W. (2009) High precision oxygen isotope analysis
788 and the effect of sample topography. *Chem. Geol.* **264**, 43-57.
789 Kita N. T., Nagahara H., Tachibana S., Tomomura S., Spicuzza M. J., Fournelle J. H. and Valley
790 J. W. (2010) High precision SIMS oxygen three isotope study of chondrules in LL3 chondrites:
791 role of ambient gas during chondrule formation. *Geochim. Cosmochim. Acta* **74**, 6610-6635.
792 Kita N. T., Ushikubo T., Knight K. B., Mendybaev R. A., Davis A. M., Richter F. M. and Fournelle
793 J. H. (2012) Internal ^{26}Al-^{26}Mg isotope systematics of a Type B CAI: Remelting of refractory
794 precursor solids. *Geochim. Cosmochim. Acta* **86**, 37-51.
795 Knight K. B., Kita N. T., Mendybaev R. A., Richter F. M., Davis A. M. and Valley J. W. (2009)
796 Silicon isotope fractionation of CAI-like vacuum evaporation residues. *Geochim. Cosmochim.*
797 *Acta* **73**, 6390–6401.

798 Krot A. A., Petaev M. I., Scott E. R. D., Choi B.-G., Zolensky M. E. and Keil K. (21998)
799 Progressive alteration in CV3 chondrites: More evidence for asteroidal alteration. *Meteorit.*
800 *Planet. Sci.* **33**, 1065-1085.
801 Krot A. N., Nagashima K., Wasserburg G. J., Huss G. R., Papanastassiou D., Davis A. M.,
802 Hutcheon I. D. and Bizzarro M. (2014) Calcium-aluminum-rich inclusions with fractionation
803 and unknown nuclear effects (FUN CAIs): I. Mineralogy, petrology, and oxygen isotopic
804 compositions. *Geochim. Cosmochim. Acta* **145**, 206–247.
805 Krot A. N., Makide K., Nagashima K., Huss G. R., Ogliore R. C., Ciesla F. J., Yang L., Hellebrand
806 E. and Gaidos E. (2012) Heterogeneous distribution of ^{26}Al at the birth of the solar system:
807 evidence from refractory grains and inclusions. *Meteorit. Planet. Sci.* **47**, 1948-1979.
808 Krot A. N., Petaev M. I., Russell S. S., Itoh S., Fagan T. J., Yurimoto H., Chizmadia L., Weisberg
809 M. K., Komatsu M., Ulyanov A. A. and Keil K. (2004) Amoeboid olivine aggregates and
810 related objects in carbonaceous chondrites: Records of nebular and asteroid processes. *Chemie*
811 *der Erde* **64**, 185-239.
812 Lee T., Mayeda T. K. and Clayton R. N. (1980) Oxygen isotopic anomalies in Allende inclusion
813 HAL. *Geophys. Res. Lett.* **7**, 493-496.
814 Lee T., Papanastassiou D. A. and Wasserburg G. J. (1976) Demonstration of ^{26}Mg excess in
815 Allende and evidence for ^{26}Al. *Geophys. Res. Lett.* **3**, 109-112.
816 Lesniak M. V. and Desch S. J. (2011) Temperature structure of protoplanetary disk undergoing
817 layered accretion. *Astrophys. J.* **740**, 514-529. p. 118 (17 pp.)
818 Liermann H.-P. and Ganguly J. (2002) Diffusion kinetics of Fe^{2+} and Mg in aluminous spinel:
819 experimental determination and applications. *Geochim. Cosmochim. Acta* **66**, 2903-2913.

820 Loss R. D., Lugmair G. W., Davis A. M. and MacPherson G. J. (1994) Isotopically distinct
821 reservoirs in the solar nebula: isotope anomalies in Vigarano meteorite inclusions. *Astrophys.*
822 *J.* **436**, L193-L196.
823 Lundstrom C. C., Sutton A. L., Chaussidon M., McDonough W. F. and Ash R. (2006) Trace
824 element partitioning between type B CAI melts and melilite and spinel: Implications for trace
825 element distribution during CAI formation. *Geochim. Cosmochim. Acta* **70**, 3421-3435.
826 MacPherson G. J., Kita N. T., Ushikubo T., Bullock E. S. and Davis A. M. (2012) Well-resolved
827 variations in the formation ages for Ca-Al-rich inclusions in the early solar system. *Earth*
828 *Planet. Sci. Lett.* **331-332**, 43-54.
829 Mendybaev R. A., Teng F.-Z., Georg R. B. and Richter F. M. (2013a) Magnesium and silicon
830 isotopic fractionations during evaporation of forsterite-rich melts: The temperature and
831 composition effects. *Lunar Planet. Sci.* **44**, #3017.
832 Mendybaev R. A., Richter F. M., Georg R. B., Janney P. E., Spicuzza M. J., Davis A. M. and
833 Valley J. W. (2013b) Experimental evaporation of Mg- and Si-rich melts: Implication for
834 the origin and evolution of FUN CAIs. *Geochim. Cosmochim. Acta* **123**, 368–384.
835 Mendybaev R. A., Williams C. D., Spicuzza M. J., Richter F. M., Valley J. W., Fedkin A. Y.,
836 and Wadhwa M. (2016) Thermal and chemical evolution of early Solar System solids as
837 seen by Allende FUN CAI CMS-1: Part II – Laboratory evaporation of potential CMS-1
838 precursor. *Geochim. Cosmochim. Acta,* 10.1016/j.gca.2016.08.034.
839 Molini-Velsko C., Mayeda T. K. and Clayton R. N. (1983) Silicon isotopes in components of the
840 Allende meteorite. *Lunar Planet. Sci. XIV* 509-510.
841 Morioka M. and Nagasawa H. (1991) Diffusion in single crystals of melilite: II. Cations. *Geochim.*
842 *Cosmochim. Acta* **55**, 751-759.

Müller T., Dohmen R., Becker H. W., ter Heege J. H. and Chakraborty S. (2013) Fe-Mg interdiffusion rates in clinopyroxene: experimental data and implications for Fe-Mg exchange geothermometers. *Contrib Mineral Petrol* **166**, 1563-1576.

Nagahara H. and Ozawa K. (1996) Evaporation of forsterite in H_2 gas. *Geochim. Cosmochim. Acta* **60**, 1445–1459.

Palme H. and Beer H. (1993) The composition of chondritic meteorites, in: H. Voigt (ed.), Londolt-Börnsten Group VI, Astronomy and Astrophysics, Instruments; Methods; Solar System, vol. 3a, Springer pp198-221.

Papanastassiou D. A., Brigham C. A. (1989) The identification of meteorite inclusions with isotope anomalies. *Astrophys. J.* **338**, L37-L40.

Richter F. M., Davis A. M., Ebel D. S. and Hashimoto A. (2002) Elemental and isotopic fractionation of Type B calcium-, aluminum-rich inclusions: experiments, theoretical considerations, and constraints on their thermal evolution. *Geochim. Cosmochim. Acta* **66**, 521–540.

Richter F. M., Mendybaev R. A. and Davis A. M. (2006) Conditions in the protoplanetary disk as seen by the type B CAIs. *Meteorit. Planet. Sci* **41**, 83-93.

Richter F. M., Janney P. E., Mendybaev R. A., Davis A. M. and Wadhwa M. (2007) Elemental and isotopic fractionation of Type B CAI-like liquids by evaporation. *Geochim. Cosmochim. Acta* **71**, 5544–5564.

Scott E. R. D., Keil K. Stöffler D. (1992) Shock metamorphism of carbonaceous chondrites. *Geochim. Cosmochim. Acta* **56**, 4281-4293.

Simon S. B., Grossman L. and Davis A. M. (1991) Fassaite composition trends during crystallization of Allende Type B refractory inclusion melts. *Geochim. Cosmochim. Acta* **55**, 2635–2655.

Srinivasani G., Juss G. R. and Wasserburg G. J. (2000) A petrographic, chemical, and isotopic study of calcium-aluminum-rich inclusions and aluminum-rich chondrules from the Axtell (CV3) chondrite. *Meteorit. Planet. Sci.* **35**, 1333-1354.

Stolper E. and Paque J.M. (1986) Crystallization sequences of Ca–Al-rich inclusions from Allende; the effects of cooling rate and maximum temperature. *Geochim. Cosmochim. Acta* **50**, 1785–1806.

Taylor S. R. and Mason B. (1978) Chemical characteristics of Ca-Al inclusions in the Allende meteorite. *Lunar Planet. Sci. IX* 1158-1160.

Tenner T. J., Ushikubo T., Kurahashi E., Kita N. T. and Nagahara H. (2013) Oxygen isotope systematics of chondrule phenocrysts from the CO3.0 chondrite Yamato 81020: Evidence for two distinct oxygen isotope reservoirs. *Geochim. Cosmochim. Acta* **102**, 226-245.

Thrane K., Nagashima K., Krot A. N. and Bizzarro M. (2008) Discovery of a new FUN CAI from a CV carboanceous chondrite: evidence for multistage thermal processing in the protoplanetary disk. *Astrophys. J.* **680**, L141-L144.

Thrane K., Bizzarro M. and Baker J. A. (2006) Extremely brief formation interval for refractory inclusions and uniform distribution of ^{26}Al in the early solar system. *Astrophys. J.* **646**, L159-L162.

Ushikubo T., Tenner T. J., Hiyagon H. and Kita N. T. (2016) A long duration of the ^{16}O-rich reservoir in the solar nebula, as recorded in fine-grained refractory inclusions from the least metamorphosed carbonaceous chondrites. *Geochim. Cosmochim. Acta* **(accepted)**.

887 Wang J., Davis A. M., Clayton R. N., Mayeda T. K. and Hashimoto A. (2001) Chemical and
888 isotopic fractionation during the evaporation of the FeO-MgO-SiO2-CaO-Al2O3-TiO2 rare
889 earth element melt system. *Geochim. Cosmochim. Acta* **65**, 479-494.
890 Wasserburg G. J., Lee T. and Papanastassiou D. A. (1977) Correlated O and Mg isotopic anomalies
891 in Allende inclusions: II. Magnesium. *Geophys. Res. Lett.* **4**, 299-302.
892 Wasserburg G. J., Wimpenny J. and Yin Q.-Z. (2012) Mg isotopic heterogeneity, Al-Mg isochron,
893 and canonical 26Al-27Al in the early solar system. *Meteorit. Planet. Sci.* **47**, 1980-1997.
894 Wasson J. T., Yurimoto H., and Russell S. S. (2001) ^{16}O-rich melilite in CO3.0 chondrites:
895 Possible formation of common ^{16}O-poor melilite by aqueous alteration. *Geochimica et*
896 *Cosmochimica Acta* **65**, 4539–4549.
897 Williams C. D., Janney P. E., Hines R. R. and Wadhwa M. (2016) Precise titanium isotope
898 compositions of refractory inclusions in the Allende CV3 chondrite by LA-MC-ICMPS. *Chem.*
899 *Geol.* **436**, 1-10..
900 Yeh H. –W. and Epstein S. (1978) 29Si/28Si and 30Si/28Si of meteorites and Allende inclusions.
901 *Lunar Planet. Sci. XVIII* 1289-1291.
902 Young E. D. and Galy A. (2004) The isotope geochemistry and cosmochemistry of magnesium.
903 *Rev. Mineral. Geochem.* **55**, 197–230.
904 Yurimoto H., Ito M., and Nagasawa H. (1998) Oxygen isotope exchange between refractory
905 inclusion in Allende and solar nebula gas. *Science* **282**, 1874–1877.
906 Zinner E. and Crozaz G. (1986) A method for the quantitative measurement of rare earth elements
907 in the ion microprobe. *Int. J. Mass Spectrom. Ion Processes* **69**, 17-38.
908

Figure 1

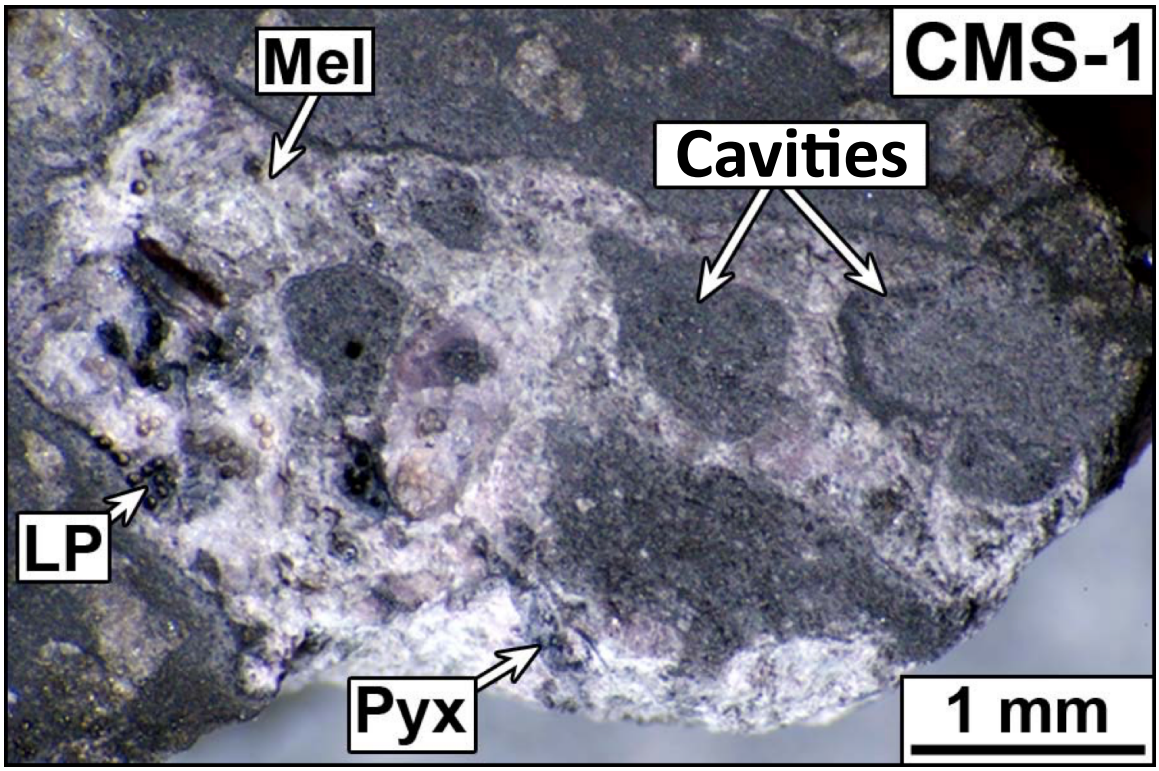

Figure 2

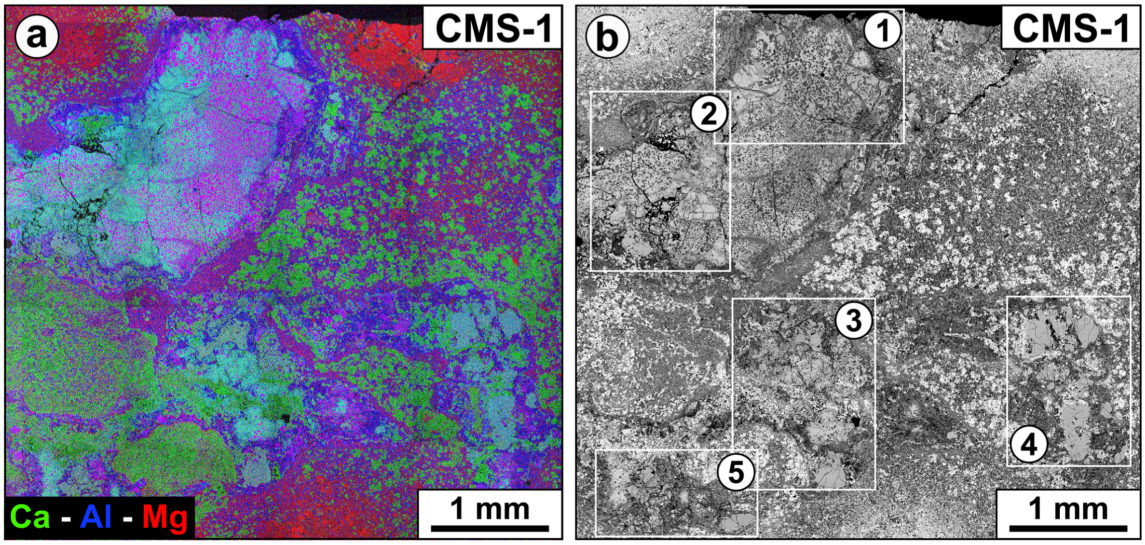

Figure 3

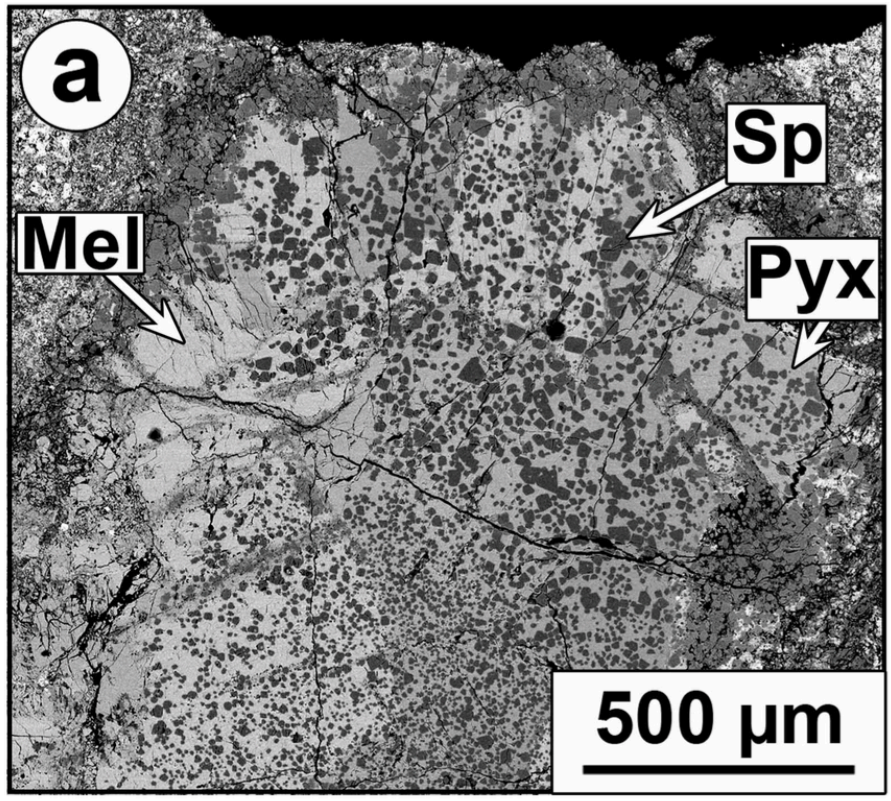

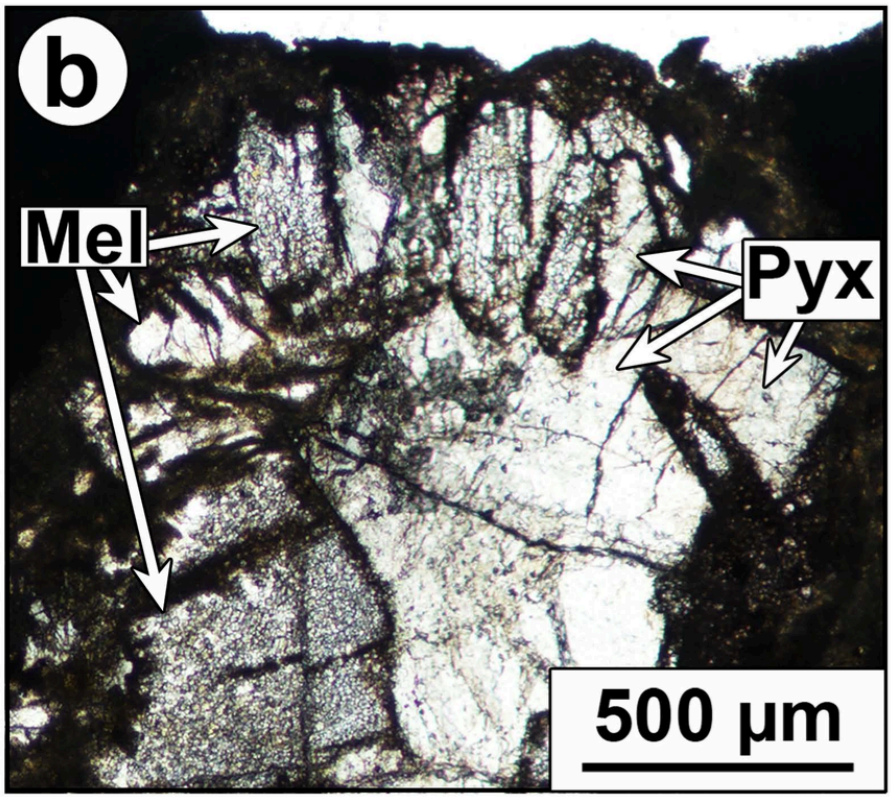

Figure 4

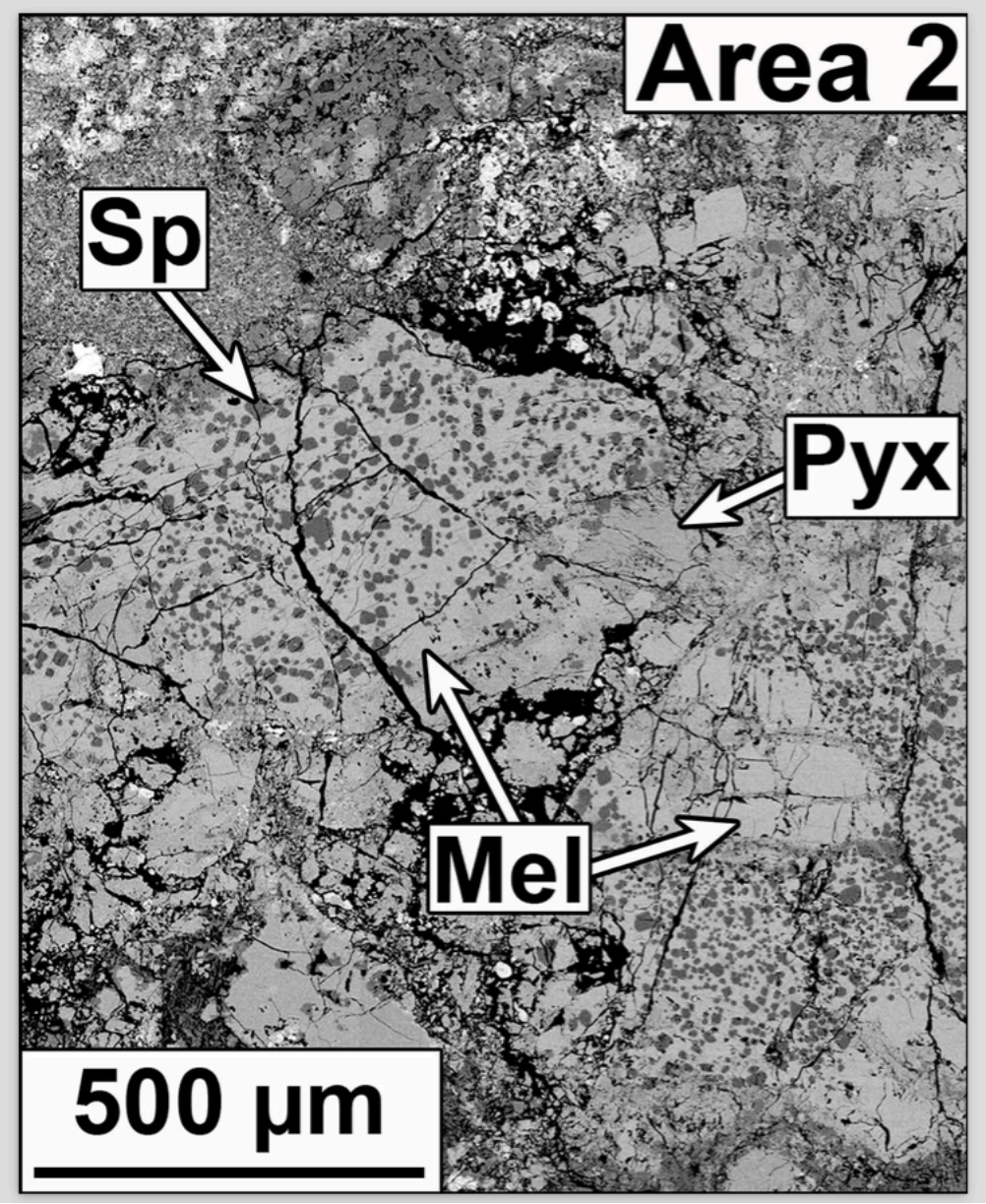

Figure 5

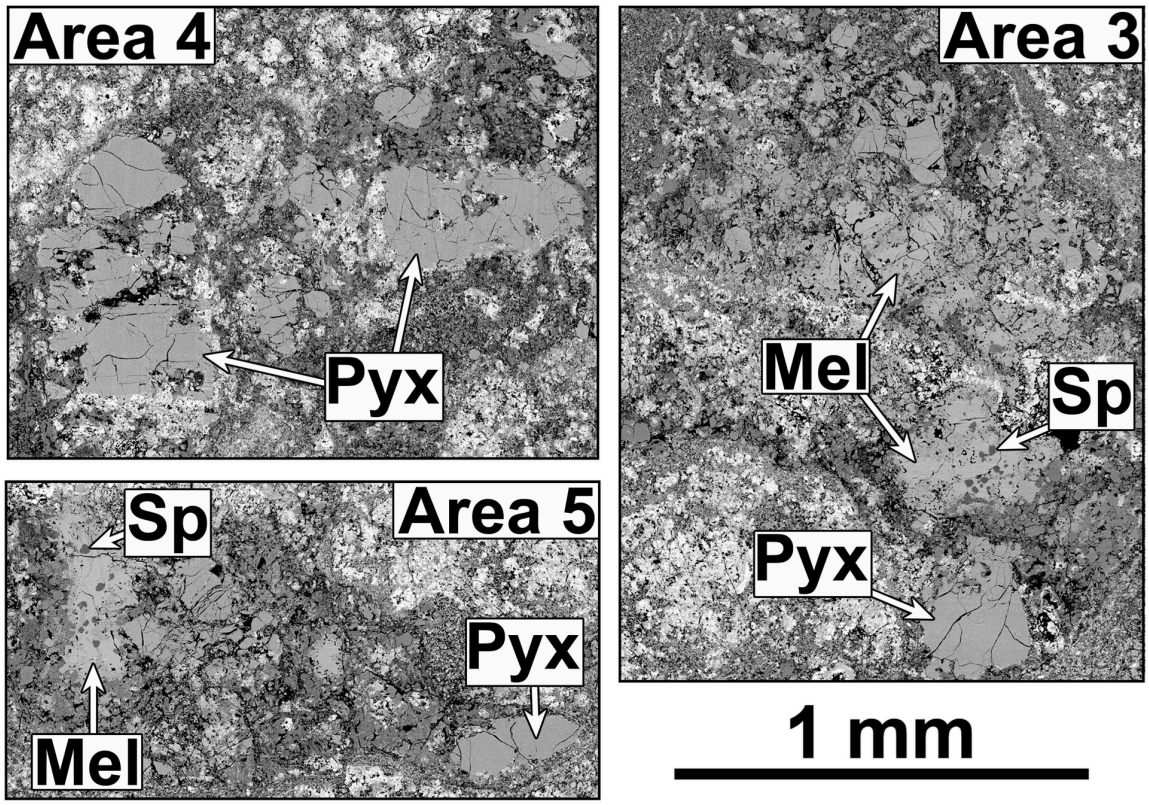

Figure 6

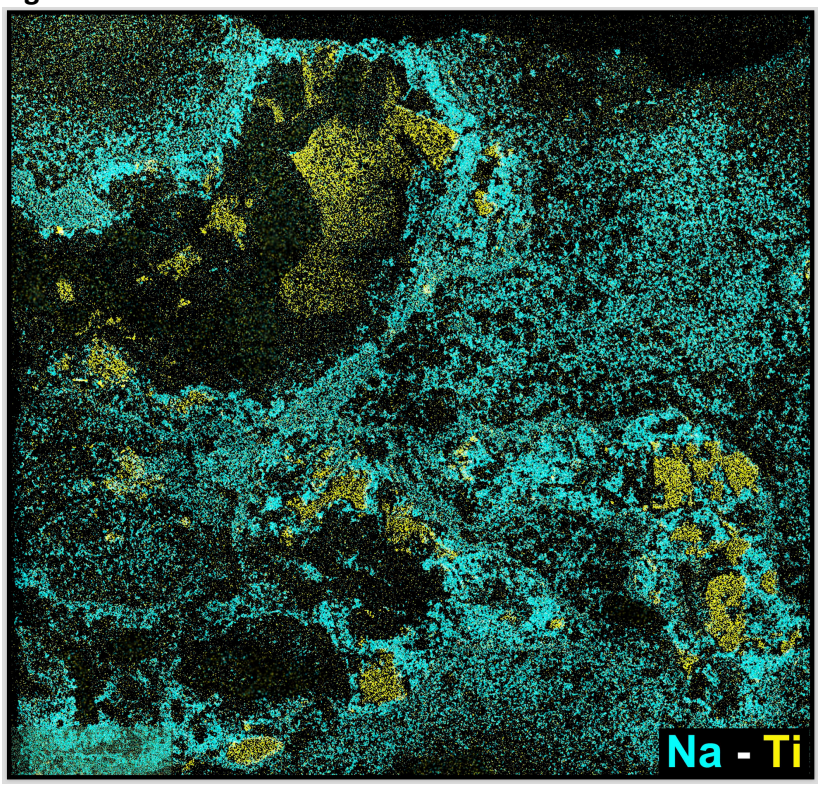

Figure 7

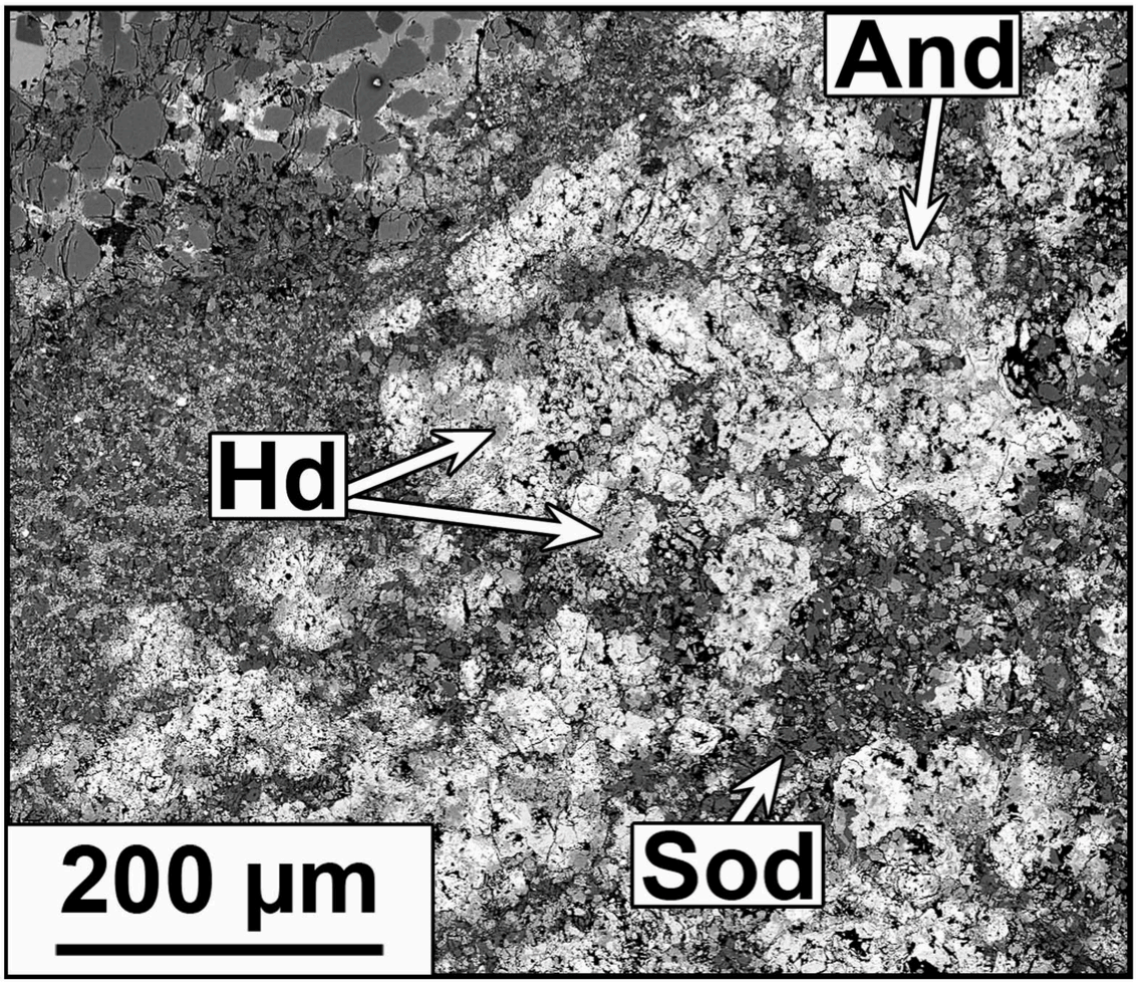

Figure 8

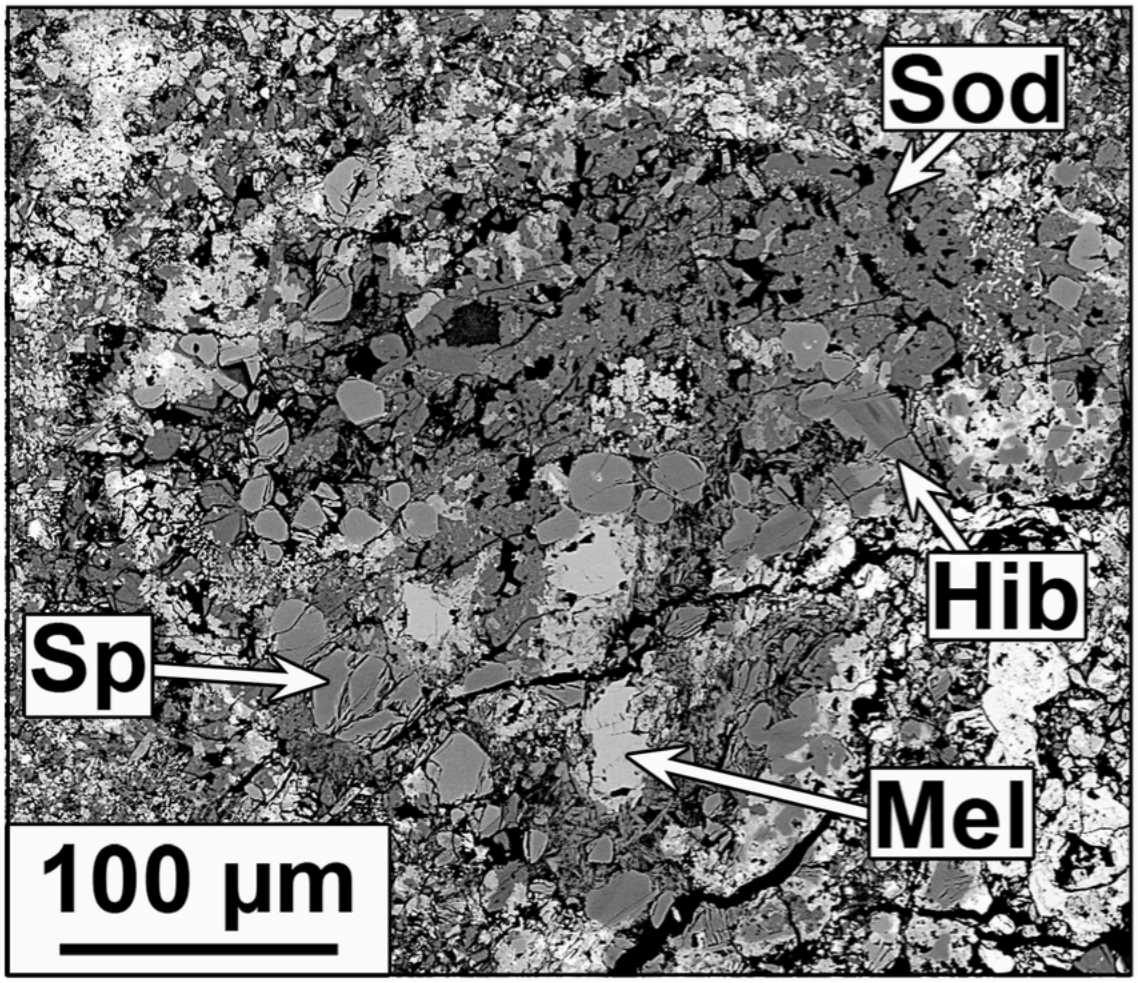

Figure 9

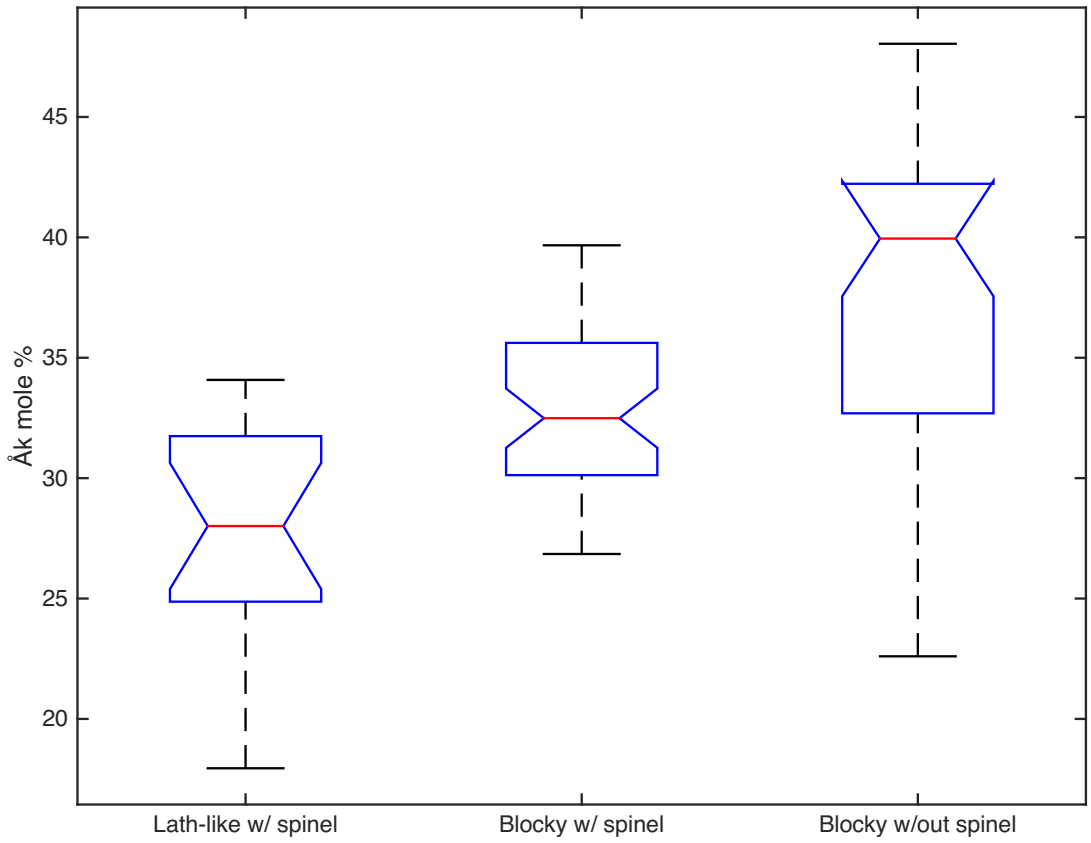
Åk mole %
45
40
35
30
25
20
Lath-like w/ spinel
Blocky w/ spinel
Blocky w/out spinel

Figure 10

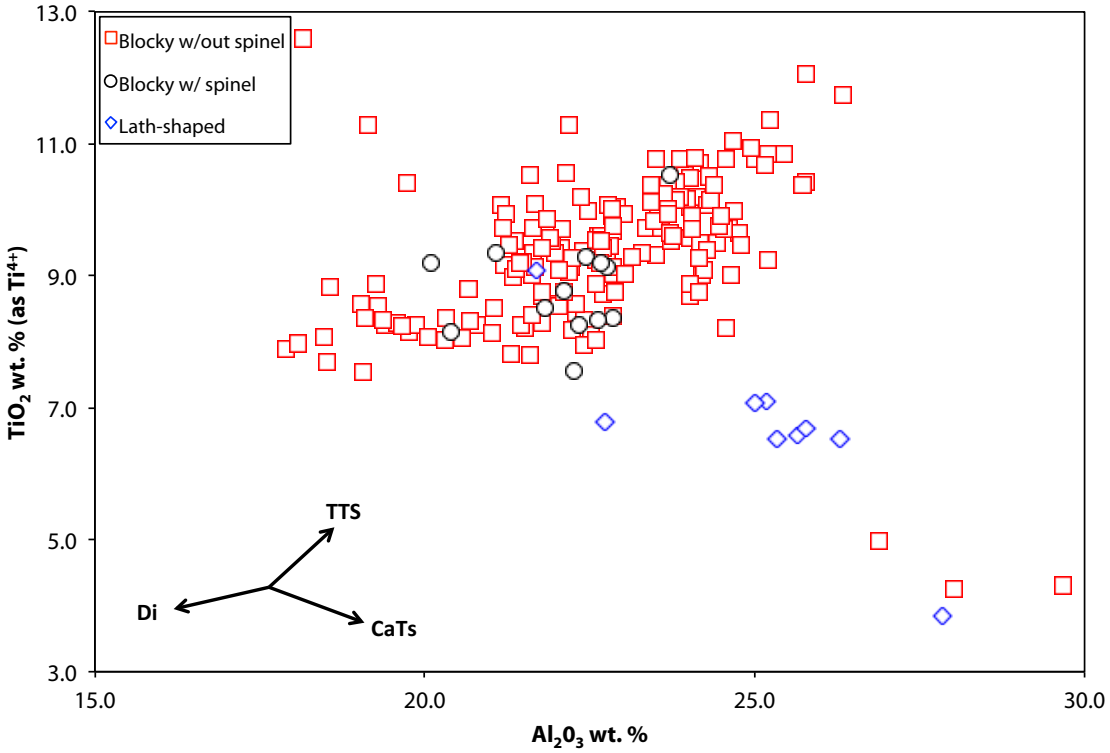
Blocky w/out spinel
Blocky w/ spinel
Lath-shaped
13.0
11.0
9.0
7.0
5.0
3.0
15.0
20.0
25.0
30.0
TiO2 wt. % (as Ti4+)
Al203 wt. %
TTS
Di
CaTs

Figure 11

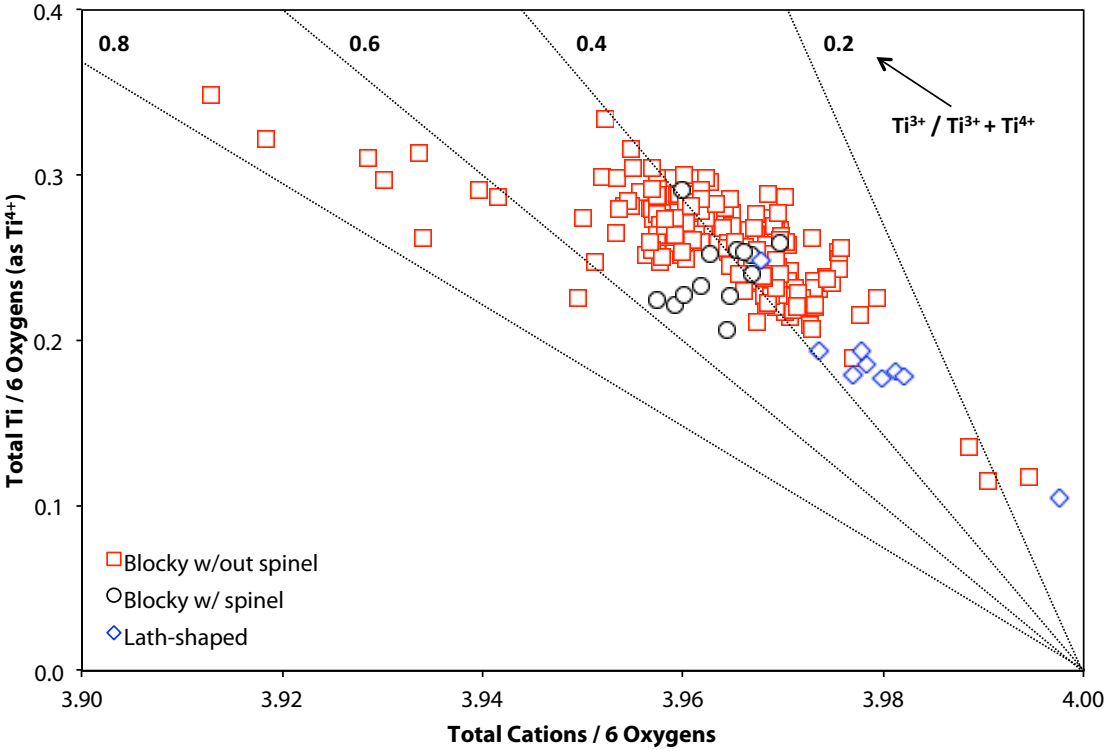
0.8
0.6
0.4
0.2
Ti3+ / Ti3+ + Ti4+
Total Ti / 6 Oxygens (as Ti4+)
Total Cations / 6 Oxygens
0.0
0.1
0.2
0.3
0.4
3.90
3.92
3.94
3.96
3.98
4.00
Blocky w/out spinel
Blocky w/ spinel
Lath-shaped

Figure 12

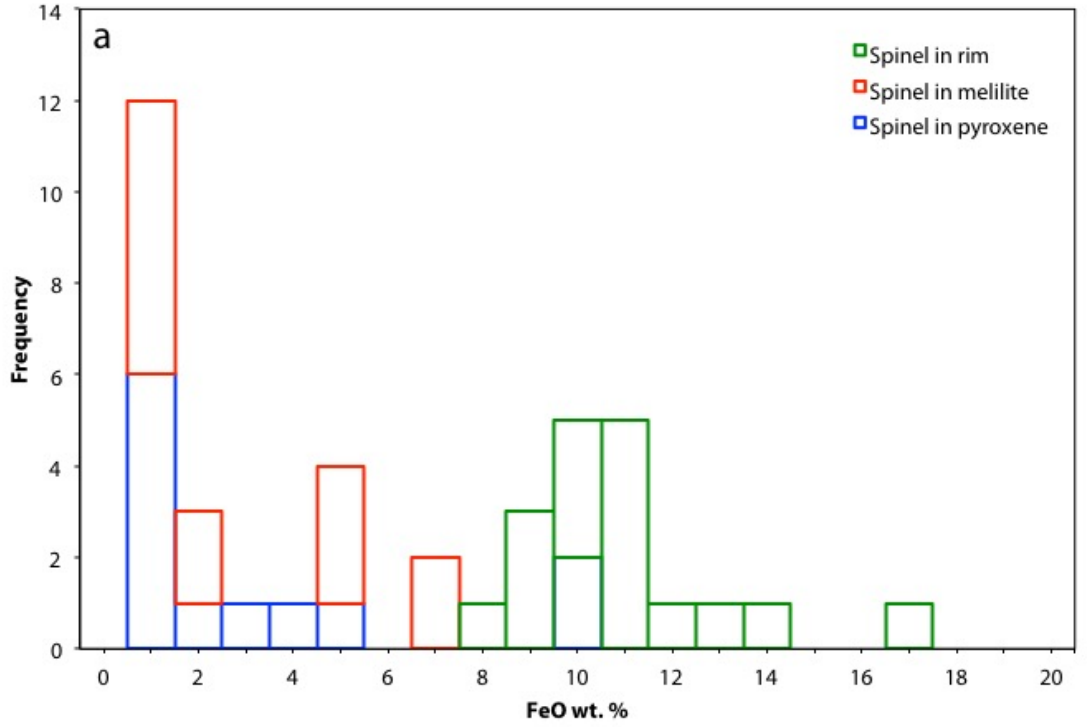
a
Spinel in rim
Spinel in melilite
Spinel in pyroxene
Frequency
FeO wt. %
0
2
4
6
8
10
12
14
16
18
20

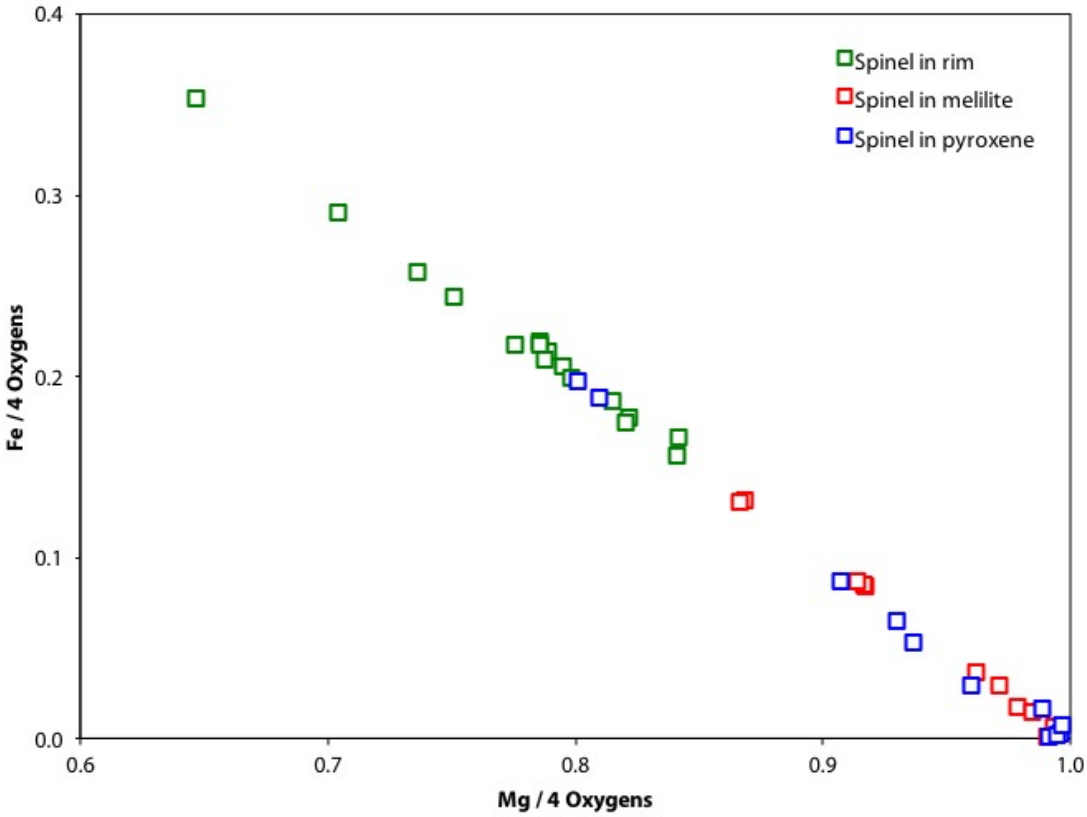
Spinel in rim
Spinel in melilite
Spinel in pyroxene
Fe / 4 Oxygens
Mg / 4 Oxygens
0.0
0.1
0.2
0.3
0.4
0.6
0.7
0.8
0.9
1.0

Figure 13

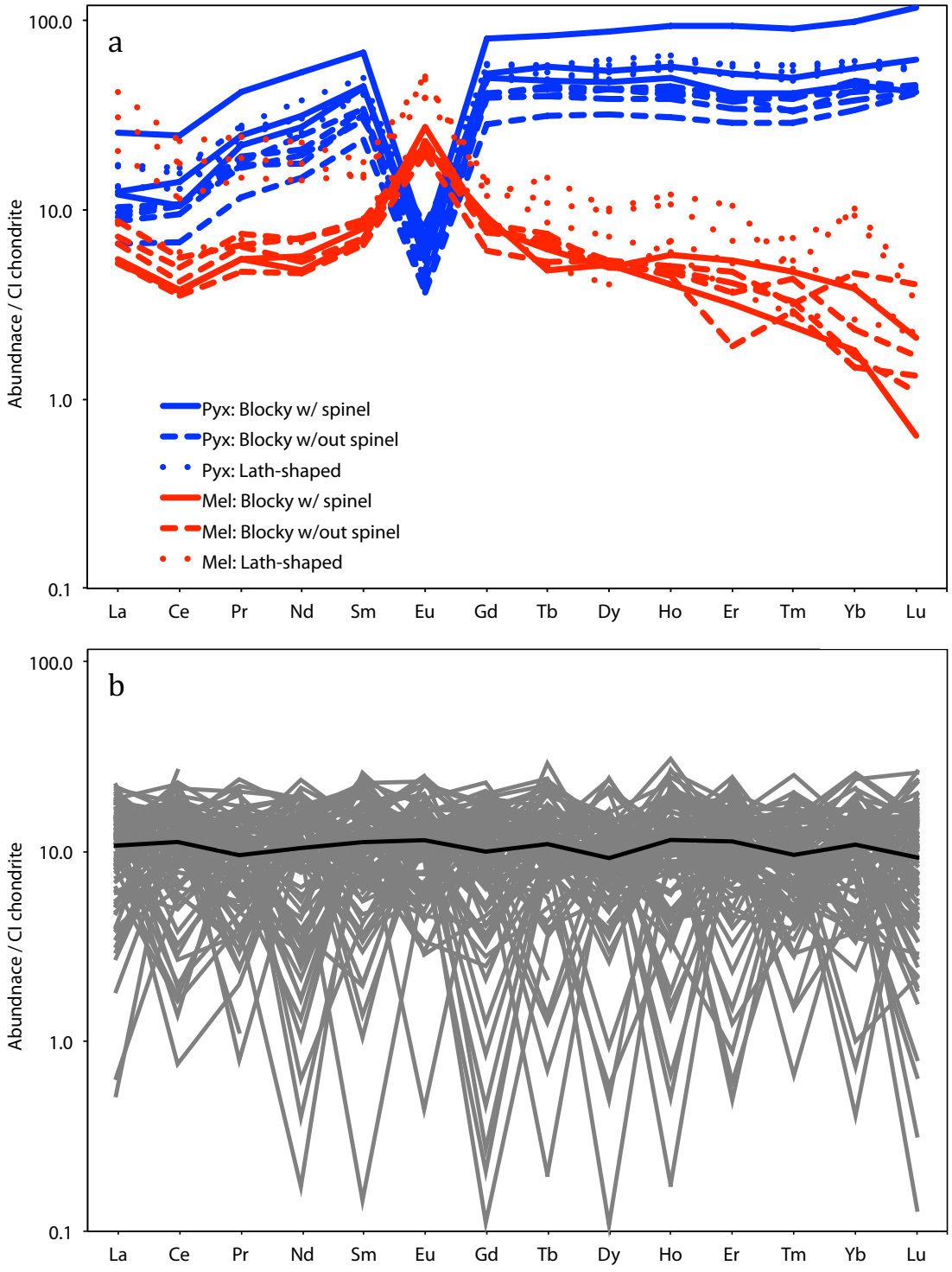
a
b
100.0
10.0
1.0
0.1
Abundnace / CI chondrite
La
Ce
Pr
Nd
Sm
Eu
Gd
Tb
Dy
Ho
Er
Tm
Yb
Lu
Pyx: Blocky w/ spinel
Pyx: Blocky w/out spinel
Pyx: Lath-shaped
Mel: Blocky w/ spinel
Mel: Blocky w/out spinel
Mel: Lath-shaped

Figure 14

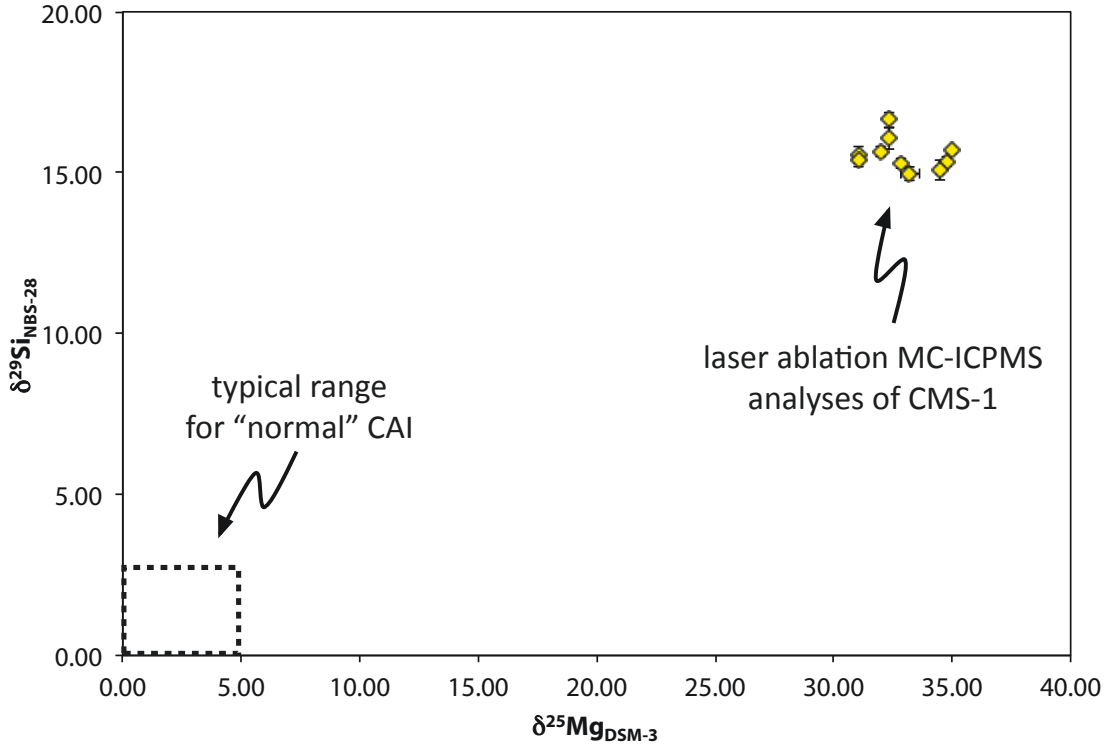
20.00
15.00
10.00
5.00
0.00
δ29SiNBS-28
0.00
5.00
10.00
15.00
20.00
25.00
30.00
35.00
40.00
δ25MgDSM-3
typical range
for "normal" CAI
laser ablation MC-ICPMS
analyses of CMS-1

Figure 15

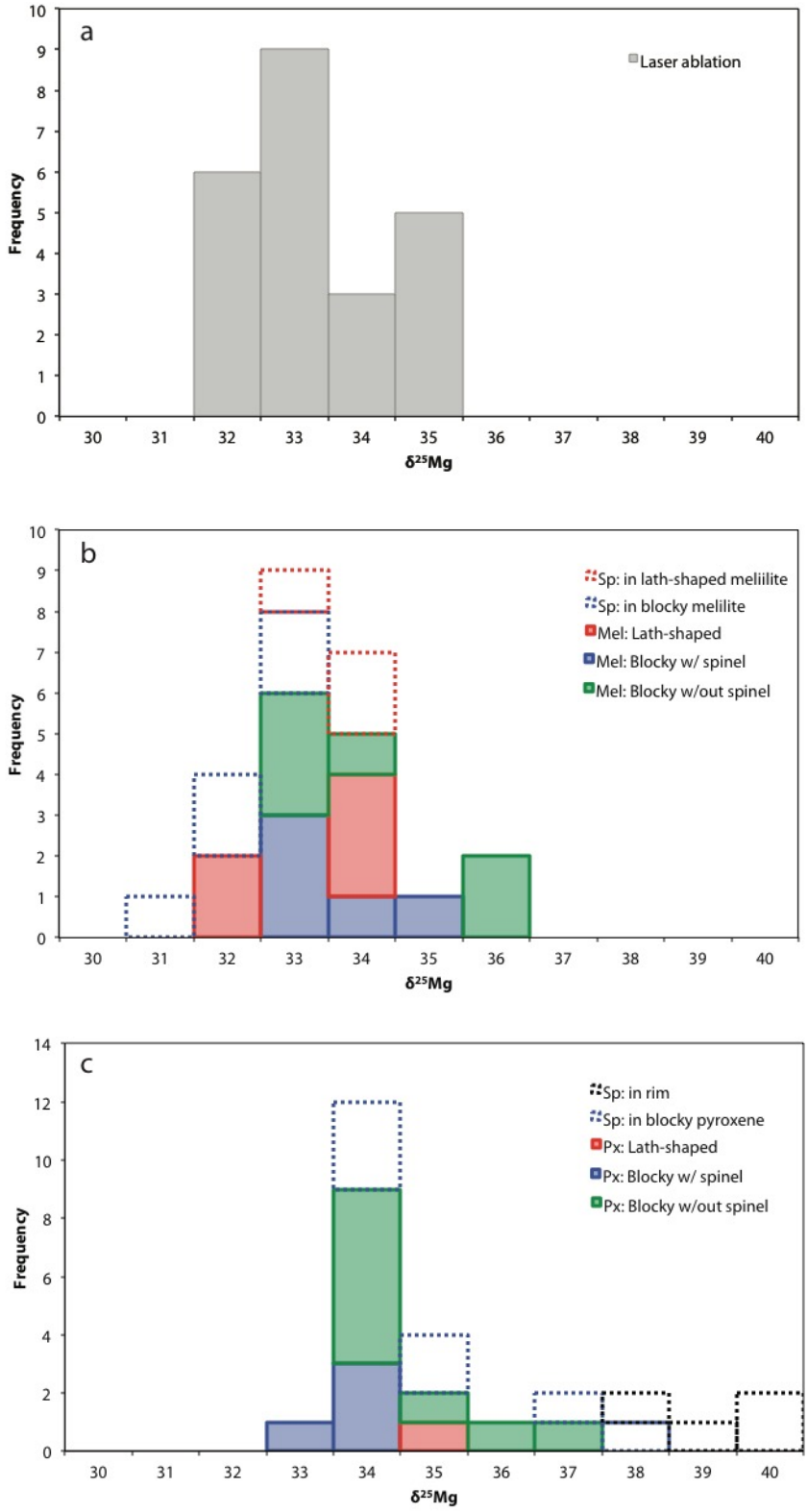
a
Laser ablation
Frequency
δ25Mg
b
Sp: in lath-shaped meliilite
Sp: in blocky melilite
Mel: Lath-shaped
Mel: Blocky w/ spinel
Mel: Blocky w/out spinel
Frequency
δ25Mg
c
Sp: in rim
Sp: in blocky pyroxene
Px: Lath-shaped
Px: Blocky w/ spinel
Px: Blocky w/out spinel
Frequency
δ25Mg

Figure 16

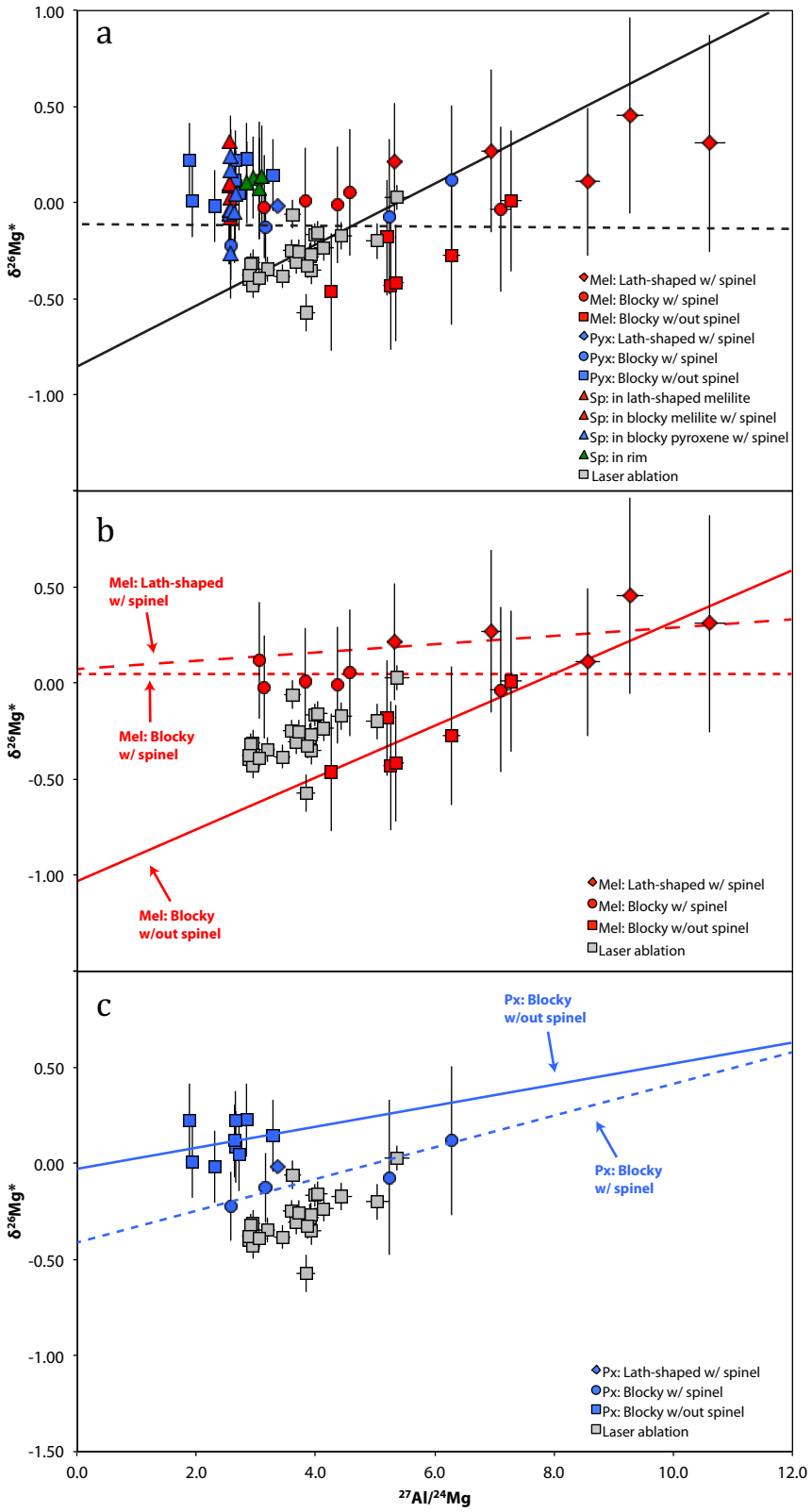
a
b
c
δ26Mg*
27Al/24Mg
1.00
0.50
0.00
-0.50
-1.00
-1.50
0.0
2.0
4.0
6.0
8.0
10.0
12.0
Mel: Lath-shaped w/ spinel
Mel: Blocky w/ spinel
Mel: Blocky w/out spinel
Pyx: Lath-shaped w/ spinel
Pyx: Blocky w/ spinel
Pyx: Blocky w/out spinel
Sp: in lath-shaped melilite
Sp: in blocky melilite w/ spinel
Sp: in blocky pyroxene w/ spinel
Sp: in rim
Laser ablation
Mel: Lath-shaped w/ spinel
Mel: Blocky w/ spinel
Mel: Blocky w/out spinel
Px: Lath-shaped w/ spinel
Px: Blocky w/ spinel
Px: Blocky w/out spinel
Px: Blocky w/out spinel
Px: Blocky w/ spinel

Figure 17

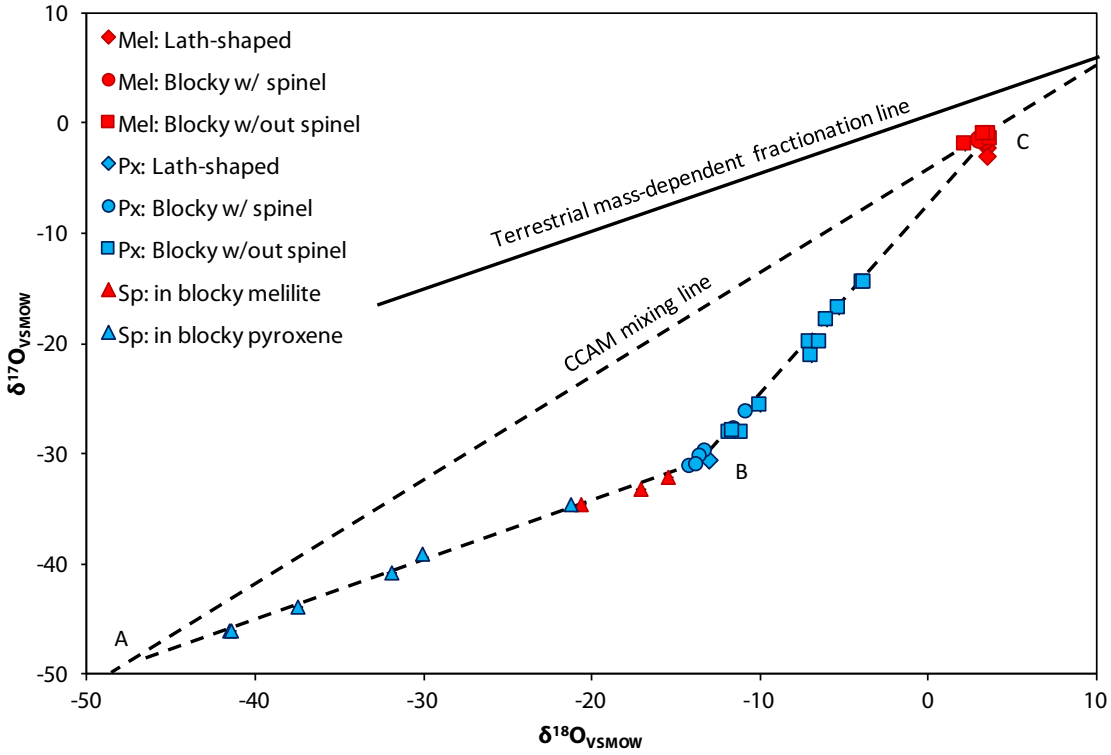
Mel: Lath-shaped
Mel: Blocky w/ spinel
Mel: Blocky w/out spinel
Px: Lath-shaped
Px: Blocky w/ spinel
Px: Blocky w/out spinel
Sp: in blocky melilite
Sp: in blocky pyroxene
Terrestrial mass-dependent fractionation line
CCAM mixing line
A
B
C
10
0
-10
-20
-30
-40
-50
-50
-40
-30
-20
-10
0
10
δ17OVSMOW
δ18OVSMOW

Figure 18

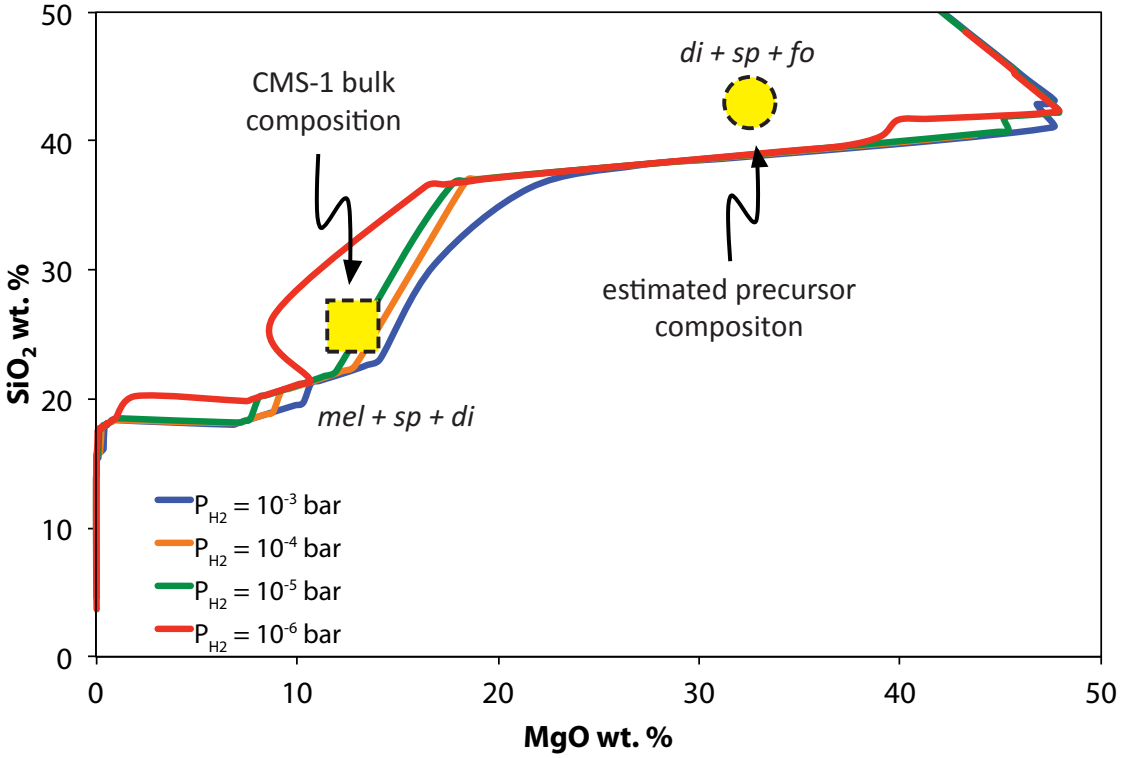
50
40
30
20
10
0
0
10
20
30
40
50
SiO2 wt. %
MgO wt. %
CMS-1 bulk composition
di + sp + fo
estimated precursor compositon
mel + sp + di
P H2 = 10-3 bar
P H2 = 10-4 bar
P H2 = 10-5 bar
P H2 = 10-6 bar

Figure 1. Incident light view of CMS-1 as it appears on the cut surface of a slab of the Allende CV3 chondrite. The lightest colored phase is melilite (Mel), black grains in the interior are pyroxene (Pyx), and the dark fine-grained material filling the large rounded regions (labeled as "cavities") is meteorite matrix and accretionary rim. The small circular features that are most prominently visible on the lower left side are laser pits (LP).

Figure 2. (a) Calcium-aluminum-magnesium X-ray map and (b) Back-scattered electron (BSE) image of the thin section of CMS-1. The numbered white squares on the BSE image are the analyzed regions of CMS-1 discussed in the text and illustrated in detail in Figs. 3-5.

Figure 3. BSE image (a) and transmitted light image (b) of Area 1 in Figure 2b . Spinel is very abundant in this region of CMS-1. Along the top edge are several lath-like melilite blades. Sp = spinel; Mel = melilite; Pyx = pyroxene.

Figure 4. BSE image of Area 2 in Figure 2b. The melilite crystals in this area are blocky in shape. Abbreviations as used in the previous figure.

Figure 5. BSE images of Areas 3, 4, and 5 in Figure 2b. Note the paucity of spinel in these regions. Abbreviations as used in previous figures.

Figure 6. Sodium and titanium X-ray map of the same region shown in Fig. 2. The titanium map shows the distribution of Ti-Al-rich primary pyroxene within the CAI, and the sodium map shows the distribution of feldspathoids (mainly sodalite) in the accretionary rim and meteorite matrix.

Figure 7. High resolution BSE image of a portion of the accretionary rim enclosing CMS-1, showing the very abundant andradite (And), hedenbergite-rich pyroxene (Hd), and sodalite (Sod).

Figure 8. Enlarged BSE image of part of Area 2 (top center on Fig. 6), showing a hibonite-bearing (Hib) nodule on the outer margin of CMS-1. Abbreviations as used previously.

Figure 9. Boxplot of compositions (Åk) of lath-shaped melilite as well as blocky melilite, with and without spinel inclusions, in CMS-1. Top and bottom of each box are the 25^{th} and 75^{th} percentiles, the red line is the median value, notches characterize the variability of the median and whiskers represent ±2.7σ. See Matlab Boxplot for further details.

Figure 10. TiO_2 vs. Al_2O_3 in the three different petrographic types of pyroxenes in CMS-1. Shown at lower-left are the compositional trends reflecting addition/subtraction of Calcium-Tschermaks pyroxene (CaTs) , diopside (Di), and Titanium-Tschermak's molecule (TTS: $CaTi^{4+}Al_2O_6$). See text for details.

Figure 11. Compositions of CMS-1 pyroxenes in terms of titanium cations per 6 oxygens plotted against total cations per 6 oxygens. Because all titanium is calculated as Ti^{4+}, any deficit in total cations is due to a net calculated excess of oxygen owing to improper valence assignment. See text for details.

Figure 12. (a) Histogram of oxidized iron contents in CMS-1 spinel and (b) Fe cations per 4 oxygens *vs.* Mg cations per 4 oxygens; the slope of the correlation line is ~ -1. Bin widths are 1 wt. %.

Figure 13. (a) Representative REE concentrations in the different petrographic types of melilite (red) and pyroxene (blue). (b) The bulk composition of CMS-1 calculated based on modal mineralogy and measured REE concentrations in its phases. The grey lines represent potential variability in the REE bulk composition of CMS-1 based on 100 Monte Carlo realizations. The solid black line represents the average of these outcomes, and is our best estimate of the bulk REE composition of CMS-1. The REE concentrations are normalized to those in CI chondrites (Palme and Beer, 1993).

Figure 14. Magnesium and silicon isotopic composition of CMS-1 measured by LA-MC-ICPMS. Also shown (box in lower left, outlined with a dashed black line) is the range of Mg and Si isotope compositions for normal CAIs.

Figure 15. Histograms displaying the magnesium isotopic compositions (a) determined by LA-MC-ICPMS; (b) of the three petrographic types of melilite, and spinel enclosed in the blocky and lath-shaped melilite, determined by SIMS; and (c) of the three petrographic types of pyroxene, and spinel enclosed in the blocky pyroxene as well as near the rim of the inclusion, determined by SIMS. Bin widths are 1‰.

Figure 16. (a) The ^{26}Al-^{26}Mg isotope systematics of CMS-1 as determined by LA-MC-ICPMS and SIMS. Solid line represents linear regression of the LA-MC-ICPMS data whereas the dashed line represents linear regression of all SIMS data. (b) The ^{26}Al-^{26}Mg isotope systematics of melilite. Lines represent linear regressions associated with distinct crystal habit. (c) The ^{26}Al-^{26}Mg isotope systematics of Ti-Al-rich pyroxene. Lines represent linear regressions associated with distinct crystal habit.

Figure 17. Oxygen isotopic compositions of individual phases from CMS-1 measured by secondary ion mass spectrometry. The trend based on analyses of spinel (AB) has a slope of ca. 0.5. The trend based on the analyses of pyroxenes and melilites (BC) has a slope of ca. 1.

Figure 18. The colored lines display the trajectories in MgO-SiO_2 space of material condensing from a gas of solar composition at different nebular pressure conditions (data of Grossman et al., 2008a extended to higher MgO and SiO2 concentrations; Mendybaev et al., 2016). Also shown is the CMS-1 bulk composition (yellow square) and its precursor composition (yellow circle) estimated using experimental data on magnesium and silicon isotope fractionation of Mendybaev et al., 2016.

Table 1

Major and minor element end-member compositions of minerals in CMS-1.

	Spinel Area 1	Spinel Area 5	Melilite Area 1	Melilite Area 2	Hibonite	Pyroxene Al-Ti-rich (min)[1] Area 3	Pyroxene Al-Ti-rich (max)[1] Area 4	Pyroxene Al-rich low-Ti[2] Area 1
SiO_2	0.00	0.00	25.79	32.91	0.00	38.63	32.71	34.87
Al_2O_3	72.22	66.04	30.37	19.57	85.00	17.89	26.34	29.67
FeO	0.09	16.48	0.02	0.01	0.26	0.04	0.06	0.01
MgO	28.54	16.96	2.53	6.73	2.43	9.78	4.95	6.48
CaO	0.07	0.08	41.79	41.95	8.50	25.74	25.54	26.03
Na_2O	0.00	0.00	0.03	0.26	0.00	0.00	0.00	0.01
K_2O	0.00	0.01	0.00	0.00	0.00	0.00	0.01	0.02
$[TiO_2]$[3]	0.12	0.22	0.03	0.06	4.51	7.90	11.74	4.31
$[TiO_2]$[4]	–	–	–	–	–	4.79	2.77	3.70
$[Ti_2O_3]$[4]	–	–	–	–	–	2.80	8.07	0.54
MnO	0.00	0.04	0.02	0.00	0.02	0.00	0.03	0.00
Cr_2O_3	0.35	0.03	0.00	0.02	0.12	0.09	0.03	0.14
Total[5]	101.39	99.87	100.58 [Åk $_{18}$]	101.51 [Åk $_{48}$]	100.84	100.08 [99.77][6]	101.42 [100.52][6]	101.55 [101.49][6]

[1]Pyroxenes with correlated Al and Ti, with minimum and maximum Ti abundances.
[2]Pyroxenes in which Al and Ti are not correlated, with highest Al abundance.
[3]All Ti calculated as Ti^{4+}.
[4]Ti^{4+} & Ti^{3+} calculated from stoichiometry (pyroxene only).
[5] Total with all Ti calculated as Ti^{4+}.
[6]Total with Ti_2O_3 & TiO_2 calculated from stoichiometry (pyroxene only).

Table 2.
The mineral weight fractions estimated from bulk composition and average compositions (wt. %) of primary and secondary phases.

	Pyroxene	Melilite	Spinel	Sodalite (Ideal)	Anorthite (Ideal)	Measured Bulk (EDS)
SiO_2	35.3	29.6	0.0			25.4
Al_2O_3	22.7	24.2	69.9	38.0	43.2	34.8
FeO	0.1	0.0	5.8	33.0	36.6	1.4
MgO	7.8	4.7	24.5			11.9
CaO	25.7	41.7	0.1		20.2	23.9
Na_2O	0.0	0.3	0.0	23.0		0.9
K_2O	0.0	0.0	0.0			0.1
TiO_2	9.2	0.1	0.2			1.1
MnO	0.0	0.0	0.0			0
Cr_2O_3	0.1	0.0	0.3			0.1
Cl_2O				5.5		0.3
Sum of oxides	100.8	100.6	101.0	99.5	100.0	99.9
Mineral Wt. Fraction	**0.30**	**0.39**	**0.24**	**0.05**	**0.02**	

Table 3.

Rare earth and trace element concentrations (in ppm) determined for melilite and Ti-Al-rich pyroxene by SIMS.

Phase	Location	Description	La	2SE	Ce	2SE	Pr	2SE	Nd	2SE	Sm	2SE	Eu	2SE	Gd	2SE	Tb	2SE	Dy	2SE	Ho	2SE	Er	2SE	Tm	2SE	Yb	2SE	Lu	2SE	Th*	2SE	U*	2SE	Th*	2SE	U*	2SE
Pyroxene	Area 1	Blocky w/ spinel	3.05	0.21	8.99	0.36	2.36	0.12	14.95	1.14	6.86	0.46	0.31	0.06	10.64	0.48	2.12	0.10	13.70	0.52	3.23	0.14	8.71	0.38	1.28	0.09	9.21	0.43	1.57	0.11	0.26	0.08	b.d.l.	-	-	-	-	-
Pyroxene	Area 1	Blocky w/ spinel	6.21	0.37	15.67	0.62	4.06	0.20	25.01	1.89	10.42	0.73	0.41	0.08	16.44	0.66	3.09	0.16	22.31	0.81	5.29	0.23	15.49	0.67	2.32	0.16	16.27	0.78	2.94	0.19	0.51	0.12	b.d.l.	-	-	-	-	-
Pyroxene	Area 1	Blocky w/ spinel	2.85	0.49	6.65	0.74	2.11	0.17	13.00	2.37	6.78	1.13	0.36	0.14	10.16	0.92	1.81	0.18	12.05	1.13	2.81	0.39	6.83	0.81	1.06	0.18	7.52	0.94	1.06	0.26	0.23	0.10	b.d.l.	-	-	-	-	-
Pyroxene	Area 1	Blocky w/out spinel	2.36	0.25	6.76	0.43	1.60	0.14	9.15	1.25	4.60	0.59	0.48	0.09	7.99	0.48	1.50	0.12	9.72	0.57	2.18	0.17	5.65	0.42	0.86	0.10	6.22	0.49	1.07	0.12	0.12	0.06	b.d.l.	-	-	-	-	-
Pyroxene	Area 2	Blocky w/out spinel	2.25	0.27	6.68	0.41	1.72	0.14	11.62	1.36	5.30	0.61	0.24	0.07	8.37	0.49	1.62	0.12	11.06	0.60	2.41	0.16	6.21	0.48	1.02	0.11	6.94	0.50	1.12	0.12	0.12	0.06	b.d.l.	-	-	-	-	-
Pyroxene	Area 3	Blocky w/out spinel	1.61	0.14	4.33	0.24	1.13	0.08	7.02	0.75	3.63	0.31	0.21	0.04	5.80	0.29	1.18	0.07	8.04	0.37	1.73	0.10	4.81	0.27	0.73	0.06	5.51	0.32	1.04	0.08	0.08	0.03	b.d.l.	-	-	-	-	-
Pyroxene	Area 5	Blocky w/out spinel	2.13	0.22	6.05	0.39	1.66	0.13	8.35	1.15	4.94	0.52	0.21	0.06	7.92	0.48	1.49	0.11	11.01	0.62	2.28	0.15	6.58	0.44	0.85	0.12	7.01	0.53	1.16	0.12	0.11	0.06	b.d.l.	-	-	-	-	-
Pyroxene	Area 1	Blocky w/out spinel	2.53	0.21	6.79	0.38	1.85	0.12	9.93	1.05	5.19	0.46	0.28	0.06	8.21	0.42	1.67	0.10	10.93	0.51	2.54	0.14	6.61	0.38	0.99	0.09	7.87	0.47	1.13	0.10	0.56	0.23	b.d.l.	-	-	-	-	-
Pyroxene	Area 1	Lath-shaped w/ spinel	3.97	0.43	9.93	0.88	2.66	0.24	17.80	2.36	7.64	0.95	0.39	0.09	12.05	0.95	2.17	0.20	15.71	1.43	3.73	0.51	9.43	0.74	1.49	0.22	9.36	1.08	1.40	0.34	0.30	0.10	b.d.l.	-	-	-	-	-
Pyroxene	Area 1	Lath-shaped w/ spinel	3.10	0.31	8.21	0.57	2.13	0.15	12.07	1.53	6.32	0.60	0.38	0.09	9.73	0.80	1.83	0.20	13.42	1.21	3.13	0.41	8.48	0.64	1.38	0.17	9.19	0.93	1.40	0.31	0.33	0.08	b.d.l.	-	-	-	-	-
Pyroxene	Area 1	Lath-shaped w/ spinel	3.14	0.29	8.19	0.59	2.34	0.22	14.68	1.74	6.24	0.56	0.33	0.09	10.02	0.79	1.99	0.15	12.36	1.21	3.25	0.42	8.73	0.75	1.22	0.15	9.28	0.93	1.46	0.31	0.31	0.07	b.d.l.	-	-	-	-	-
Pyroxene	Area 1	Lath-shaped w/ spinel	4.02	0.34	10.69	0.74	2.59	0.19	14.46	1.93	6.96	0.47	0.43	0.10	11.86	1.06	2.14	0.17	14.65	1.24	3.42	0.46	9.82	0.85	1.49	0.19	10.03	1.01	1.52	0.33	0.78	0.11	b.d.l.	-	-	-	-	-
Pyroxene	Area 1	Blocky w/ spinel	-	-	-	-	-	-	-	-	-	-	-	-	-	-	-	-	-	-	-	-	-	-	-	-	-	-	-	-	0.13	0.03	b.d.l.	-	0.14	0.04	b.d.l.	-
Pyroxene	Area 1	Blocky w/ spinel	-	-	-	-	-	-	-	-	-	-	-	-	-	-	-	-	-	-	-	-	-	-	-	-	-	-	-	-	0.14	0.03	b.d.l.	-	0.19	0.04	b.d.l.	-
Pyroxene	Area 1	Lath-shaped w/ spinel	-	-	-	-	-	-	-	-	-	-	-	-	-	-	-	-	-	-	-	-	-	-	-	-	-	-	-	-	0.19	0.03	b.d.l.	-	0.29	0.05	b.d.l.	-
Melilite	Area 1	Blocky w/ spinel	1.28	0.17	2.37	0.29	0.52	0.07	2.68	0.65	1.23	0.26	1.25	0.15	1.87	0.22	0.18	0.04	1.31	0.23	0.23	0.05	0.53	0.12	0.06	0.02	0.30	0.08	0.02	0.01	0.06	0.04	b.d.l.	-	-	-	-	-
Melilite	Area 2	Blocky w/ spinel	1.34	0.19	2.41	0.27	0.53	0.08	2.25	0.66	1.08	0.26	1.59	0.18	1.67	0.23	0.23	0.05	1.27	0.22	0.33	0.06	0.89	0.18	0.12	0.03	0.63	0.15	0.05	0.02	0.00	0.00	b.d.l.	-	-	-	-	-
Melilite	Area 1	Blocky w/out spinel	1.55	0.15	2.65	0.22	0.62	0.06	2.52	0.50	1.08	0.12	1.28	0.09	1.55	0.17	0.26	0.03	1.38	0.18	0.27	0.04	0.60	0.10	0.11	0.02	0.39	0.07	0.04	0.01	0.05	0.02	b.d.l.	-	-	-	-	-
Melilite	Area 1	Blocky w/out spinel	1.71	0.19	3.18	0.28	0.72	0.07	3.32	0.68	1.29	0.23	1.31	0.13	1.69	0.19	0.25	0.04	1.27	0.17	0.27	0.05	0.69	0.12	0.08	0.02	0.28	0.07	0.03	0.01	0.10	0.06	b.d.l.	-	-	-	-	-
Melilite	Area 1	Blocky w/out spinel	2.03	0.20	3.55	0.32	0.62	0.07	3.37	0.60	1.37	0.22	1.33	0.13	1.72	0.20	0.28	0.04	1.25	0.18	0.34	0.06	0.61	0.10	0.07	0.02	0.43	0.08	0.06	0.02	0.04	0.02	b.d.l.	-	-	-	-	-
Melilite	Area 2	Blocky w/out spinel	1.28	0.16	2.24	0.22	0.45	0.06	2.20	0.52	1.01	0.21	1.15	0.12	1.24	0.16	0.20	0.04	1.36	0.18	0.29	0.05	0.78	0.13	0.08	0.02	0.76	0.14	0.10	0.03	0.04	0.03	b.d.l.	-	-	-	-	-
Melilite	Area 1	Lath-shaped	4.77	0.38	7.24	0.50	1.43	0.12	6.75	0.85	2.35	0.30	2.29	0.15	2.88	0.29	0.32	0.04	1.82	0.21	0.39	0.06	0.86	0.14	0.14	0.03	0.65	0.13	0.06	0.02	0.17	0.05	b.d.l.	-	-	-	-	-
Melilite	Area 1	Lath-shaped	2.07	0.22	3.80	0.46	0.67	0.08	3.20	0.69	1.38	0.28	1.52	0.16	1.81	0.21	0.19	0.04	1.02	0.16	0.28	0.05	0.40	0.10	0.05	0.02	0.33	0.09	0.04	0.02	0.08	0.05	b.d.l.	-	-	-	-	-
Melilite	Area 1	Lath-shaped	7.53	0.37	11.26	0.46	1.81	0.12	8.30	0.98	2.27	0.30	2.82	0.19	2.90	0.21	0.41	0.05	2.47	0.21	0.61	0.07	1.14	0.15	0.18	0.03	1.54	0.19	0.08	0.02	0.92	0.16	b.d.l.	-	-	-	-	-
Melilite	Area 1	Lath-shaped	10.25	0.49	14.80	0.64	2.34	0.16	10.79	1.35	2.76	0.39	2.92	0.20	2.41	0.20	0.56	0.06	2.56	0.25	0.69	0.08	1.73	0.21	0.12	0.03	1.68	0.27	0.10	0.03	0.82	0.16	b.d.l.	-	-	-	-	-
Melilite	Area 1	Blocky w/out spinel	-	-	-	-	-	-	-	-	-	-	-	-	-	-	-	-	-	-	-	-	-	-	-	-	-	-	-	-	0.04	0.02	b.d.l.	-	0.07	0.03	b.d.l.	-
Melilite	Area 1	Lath-shaped w/ spinel	-	-	-	-	-	-	-	-	-	-	-	-	-	-	-	-	-	-	-	-	-	-	-	-	-	-	-	-	b.d.l.	-	b.d.l.	-	b.d.l.	-	b.d.l.	-
Est. bulk comp.			1.88	1.05	3.77	1.62	0.85	0.30	4.61	1.69	2.09	0.54	1.09	0.21	3.05	0.81	0.51	0.14	3.16	1.07	0.76	0.27	1.91	0.82	0.28	0.12	1.92	0.82	0.27	0.15	0.09	0.11	b.d.l.	-	0.08	0.06	b.d.l.	-

b.d.l. refers to analyses below the detection limit of the technique, whereas dashed lines represent analyses where those particular measurements were not made or the uncertainty is associated with values below the detection limits.

The quoted 2SE uncertainties on concentrations are from counting statististics only.

*Thorium and uranium abundances determined using atomic species (see section 2 on Methods for details).

**Thorium and uranium abundances determined using monoxide species (see section 2 on Methods for details).

Table 4
Magnesium and sillicon isotope compositions (relative to the DSM-3 and NBS-28 standards, respectively) of CMS-1 via LA-MC-ICPMS.

Phase	$^{27}Al/^{24}Mg$	2SE	$\delta^{25}Mg$	2SE	$\delta^{26}Mg^*$	2SE
Mg Spot #1	3.84	0.15	33.22	0.41	-0.57	0.10
Mg Spot #2	3.93	0.16	34.81	0.14	-0.35	0.07
Mg Spot #3	2.95	0.12	32.00	0.12	-0.31	0.07
Mg Spot #4	2.91	0.12	32.36	0.05	-0.32	0.06
Mg Spot #5	2.89	0.12	32.36	0.06	-0.40	0.05
Mg Spot #6	2.95	0.12	31.08	0.10	-0.43	0.06
Mg Spot #7	3.19	0.13	31.05	0.06	-0.35	0.06
Mg Spot #8	2.89	0.12	32.85	0.06	-0.38	0.06
Mg Spot #9	3.05	0.12	34.49	0.15	-0.39	0.06
Mg Spot #10	3.44	0.14	35.00	0.07	-0.38	0.06
Mg Spot #11	3.67	0.15	34.55	0.17	-0.30	0.06
Mg Spot #12	4.43	0.18	32.75	0.21	-0.17	0.07
Mg Spot #13	5.36	0.21	32.20	0.06	0.03	0.07
Mg Spot #14	3.60	0.14	32.06	0.05	-0.25	0.06
Mg Spot #15	3.61	0.14	32.32	0.18	-0.06	0.08
Mg Spot #16	3.98	0.16	32.63	0.12	-0.17	0.06
Mg Spot #17	3.90	0.16	32.98	0.28	-0.28	0.07
Mg Spot #18	4.14	0.17	31.62	0.09	-0.23	0.07
Mg Spot #19	3.92	0.16	32.00	0.16	-0.27	0.07
Mg Spot #20	3.86	0.15	33.37	0.06	-0.33	0.07
Mg Spot #21	5.04	0.20	31.73	0.37	-0.20	0.09
Mg Spot #22	3.72	0.15	33.95	0.08	-0.26	0.06
Mg Spot #23	4.04	0.16	34.66	0.07	-0.16	0.06
			$\delta^{29}Si$	2SE	$\delta^{30}Si$	2SE
Si Spot #1			14.98	0.23	29.30	0.18
Si Spot #2			15.34	0.14	30.02	0.19
Si Spot #3			15.67	0.16	30.52	0.16
Si Spot #4			16.07	0.33	31.54	0.18
Si Spot #5			16.65	0.23	32.28	0.24
Si Spot #6			15.54	0.25	30.25	0.25
Si Spot #7			15.38	0.19	29.95	0.18
Si Spot #8			15.28	0.14	29.81	0.20
Si Spot #9			15.08	0.31	29.48	0.14
Si Spot #10			15.68	0.11	30.47	0.10

Table 5

Magnesium isotope compositions (reported relative to DSM-3) of minerals in CMS-1 via SIMS.

Phase	Location	Description	$^{27}Al/^{24}Mg$	2SE	$\delta^{25}Mg$	2SE	$\delta^{26}Mg$*	2SE
Melilite-Åk28	Area 1	Lath-shaped w/ spinel	6.94	0.17	31.67	0.43	0.11	0.42
Melilite-Åk33	Area 1	Lath-shaped w/ spinel	5.33	0.13	31.74	0.43	0.06	0.30
Melilite-Åk19.6	Area 1	Lath-shaped w/ spinel	8.56	0.21	33.34	0.43	-0.06	0.39
Melilite-Åk19.3	Area 1	Lath-shaped w/ spinel	10.61	0.26	33.53	0.43	0.14	0.57
Melilite-Åk20.9	Area 1	Lath-shaped w/ spinel	9.27	0.23	33.11	0.25	0.29	0.51
Melilite-Åk48	Area 2	Blocky w/ spinel	3.06	0.08	31.01	0.43	-0.04	0.30
Melilite-Åk37	Area 5	Blocky w/ spinel	4.37	0.11	33.98	0.43	-0.18	0.31
Melilite-Åk35.6	Area 4	Blocky w/ spinel	4.58	0.11	31.54	0.43	-0.10	0.33
Melilite-Åk26.3	Area 4	Blocky w/ spinel	7.10	0.17	32.10	0.43	-0.19	0.43
Melilite-Åk42	Area 1	Blocky w/ spinel	3.14	0.08	31.34	0.25	-0.18	0.27
Melilite-Åk40.2	Area 1	Blocky w/ spinel	3.82	0.09	30.71	0.25	-0.14	0.27
Melilite-Åk30	Area 1	Blocky w/out spinel	7.28	0.18	33.33	0.43	-0.15	0.37
Melilite-Åk28	Area 2	Blocky w/out spinel	5.20	0.13	32.29	0.43	-0.34	0.30
Melilite-Åk33	Area 2	Blocky w/out spinel	5.26	0.13	32.99	0.43	-0.59	0.34
Melilite-Åk40	Area 2	Blocky w/out spinel	4.27	0.10	35.01	0.43	-0.64	0.31
Melilite-Åk40	Area 5	Blocky w/out spinel	5.35	0.13	35.37	0.43	-0.59	0.31
Melilite-Åk32	Area 1	Blocky w/out spinel	6.28	0.15	32.48	0.25	-0.44	0.36
Melilite-Åk48.8	Area 1	Blocky w/out spinel	2.65	0.06	36.60	0.25	0.03	0.16
Pyroxene-TiO_2=6.5	Area 1	Lath-shaped w/ spinel	3.36	0.05	34.22	0.54	-0.19	0.19
Pyroxene-TiO_2=9.8	Area 1	Blocky w/ spinel	3.34	0.05	33.33	0.54	0.03	0.19
Pyroxene-TiO_2=8.4	Area 3	Blocky w/ spinel	6.29	0.09	33.55	0.54	-0.05	0.39
Pyroxene-TiO_2=9.7	Area 3	Blocky w/ spinel	5.23	0.07	32.75	0.54	-0.24	0.40
Pyroxene-TiO_2=4.5	Area 1	Blocky w/ spinel	2.58	0.04	33.41	0.79	-0.39	0.18
Pyroxene-TiO_2=4.5	Area 1	Blocky w/ spinel	3.16	0.04	33.42	0.79	-0.30	0.18
Pyroxene-TiO_2=2.9	Area 2	Blocky w/out spinel	2.66	0.04	33.11	0.54	-0.08	0.19
Pyroxene-TiO_2=8	Area 2	Blocky w/out spinel	2.31	0.03	33.96	0.54	-0.19	0.19
Pyroxene-TiO_2=8.8	Area 3	Blocky w/out spinel	1.88	0.03	33.95	0.54	0.06	0.19
Pyroxene-TiO_2=10	Area 3	Blocky w/out spinel	1.93	0.03	33.89	0.54	-0.16	0.19
Pyroxene-TiO_2=9.6	Area 4	Blocky w/out spinel	2.65	0.04	35.00	0.54	-0.06	0.19
Pyroxene-TiO_2=10	Area 4	Blocky w/out spinel	3.28	0.04	35.20	0.54	-0.03	0.19
Pyroxene-TiO_2=9	Area 5	Blocky w/out spinel	2.84	0.04	33.95	0.54	0.06	0.19
Pyroxene-TiO_2=5.0	Area 2	Blocky w/out spinel	2.71	0.04	33.32	0.79	-0.12	0.19
Pyroxene-TiO_2=9.3	Area 2	Blocky w/out spinel	1.99	0.03	34.15	0.79	-0.24	0.18
Spinel in Melilite	Area 1	In lath-shaped melilite	2.57	0.03	32.49	0.25	-0.12	0.26
Spinel in Melilite	Area 1	In lath-shaped melilite	2.56	0.03	33.75	0.25	-0.20	0.26
Spinel in Melilite	Area 1	In lath-shaped melilite	2.56	0.03	33.13	0.25	-0.21	0.26
Spinel in Melilite	Area 2	In blocky melilite	2.57	0.03	30.98	0.25	-0.19	0.26
Spinel in Melilite	Area 2	In blocky melilite	2.55	0.03	32.54	0.25	0.16	0.26
Spinel in Melilite	Area 2	In blocky melilite	2.55	0.03	31.97	0.25	-0.06	0.26
Spinel in Melilite	Area 2	In blocky melilite	2.55	0.03	31.80	0.25	-0.06	0.26
Spinel in Melilite	Area 1	In blocky melilite	2.57	0.03	32.31	0.17	-0.23	0.21
Spinel in pyroxene	Area 1	In blocky pyroxene	2.58	0.03	34.40	0.17	0.01	0.21
Spinel in pyroxene	Area 1	In blocky pyroxene	2.57	0.03	34.06	0.17	-0.43	0.24
Spinel in pyroxene	Area 1	In blocky pyroxene	2.65	0.03	36.13	0.25	-0.23	0.27
Spinel in pyroxene	Area 1	In blocky pyroxene	2.65	0.03	37.48	0.25	-0.13	0.27
Spinel in pyroxene	Area 1	In blocky pyroxene	2.55	0.03	33.63	0.25	-0.22	0.26
Spinel in pyroxene	Area 1	In blocky pyroxene	2.57	0.03	33.70	0.17	0.08	0.21
Spinel in pyroxene	Area 1	In blocky pyroxene	2.57	0.03	33.77	0.17	-0.20	0.21
Spinel in rim	Area 1		3.10	0.03	39.26	0.25	-0.05	0.27
Spinel in rim	Area 1		3.05	0.03	39.15	0.25	-0.11	0.27
Spinel in rim	Area 1		2.95	0.03	37.99	0.17	-0.05	0.21
Spinel in rim	Area 1		2.84	0.04	38.02	0.17	-0.08	0.21

* Pyroxene TiO_2 contents are in weight percent.

Table 6

Oxygen isotopic compositions (VSMOW) of minerals in CMS-1 via SIMS.

Phase	Location	Description	$\delta^{18}O$	2SD	$\delta^{17}O$	2SD	$\Delta^{17}O$	2SD
Spinel	Area 2	in blocky melilite	-15.40	0.26	-32.17	0.54	-24.16	0.57
Spinel	Area 2	in blocky melilite	-20.59	0.26	-34.62	0.54	-23.92	0.57
Spinel	Area 5	in blocky melilite	-17.10	0.30	-33.23	0.49	-24.34	0.54
Spinel	Area 1	in blocky pyroxene	-41.57	0.14	-46.14	0.54	-24.53	0.55
Spinel	Area 1	in blocky pyroxene	-30.07	0.14	-39.14	0.54	-23.50	0.55
Spinel	Area 1	in blocky pyroxene	-21.23	0.14	-34.66	0.54	-23.61	0.55
Spinel	Area 1	in blocky pyroxene	-37.48	0.30	-43.85	0.49	-24.36	0.54
Spinel	Area 1	in blocky pyroxene	-31.84	0.30	-40.90	0.49	-24.34	0.54
Spinel	Area 1	in blocky pyroxene	-41.42	0.30	-46.04	0.49	-24.50	0.54
Melilite-Åk28	Area 1	Lath-shaped	3.57	0.14	-3.01	0.54	-4.87	0.55
Melilite-Åk24	Area 1	Lath-shaped	3.56	0.26	-2.19	0.54	-4.04	0.57
Melilite-Åk27	Area 1	Lath-shaped	3.42	0.26	-1.83	0.54	-3.61	0.57
Melilite-Åk30	Area 1	Blocky w/ spinel	3.56	0.14	-1.10	0.54	-2.96	0.55
Melilite-Åk28	Area 2	Blocky w/ spinel	3.10	0.26	-1.64	0.54	-3.25	0.57
Melilite-Åk32	Area 1	Blocky w/out spinel	3.77	0.14	-1.47	0.54	-3.43	0.55
Melilite-Åk34	Area 2	Blocky w/out spinel	3.63	0.26	-0.97	0.54	-2.86	0.57
Melilite-Åk33	Area 2	Blocky w/out spinel	3.37	0.26	-1.02	0.54	-2.77	0.57
Melilite-Åk30	Area 2	Blocky w/out spinel	2.17	0.26	-2.02	0.54	-3.14	0.57
Pyroxene-TiO_2=6.7	Area 1	Lath-shaped w/ spinel	-13.04	0.14	-30.65	0.54	-23.87	0.55
Pyroxene-TiO_2=9.8	Area 1	Blocky w/ spinel	-10.74	0.14	-26.25	0.54	-20.67	0.55
Pyroxene-TiO_2=4.3	Area 1	Blocky w/ spinel	-13.16	0.14	-29.88	0.54	-23.04	0.55
Pyroxene-TiO_2=9.0	Area 1	Blocky w/ spinel	-11.50	0.14	-27.88	0.54	-21.90	0.55
Pyroxene-TiO_2=4.3	Area 1	Blocky w/ spinel	-13.46	0.30	-30.26	0.49	-23.26	0.54
Pyroxene-TiO_2=4.5	Area 1	Blocky w/ spinel	-14.16	0.30	-31.25	0.49	-23.89	0.54
Pyroxene-TiO_2=4.5	Area 1	Blocky w/ spinel	-13.74	0.30	-31.11	0.49	-23.96	0.54
Pyroxene-TiO_2=8.4	Area 1	Blocky w/out spinel	-5.30	0.14	-16.83	0.54	-14.08	0.55
Pyroxene-TiO_2=8.8	Area 1	Blocky w/out spinel	-6.97	0.26	-19.96	0.54	-16.33	0.57
Pyroxene-TiO_2=9.7	Area 1	Blocky w/out spinel	-9.97	0.26	-25.68	0.54	-20.50	0.57
Pyroxene-TiO_2=9.3	Area 2	Blocky w/out spinel	-3.85	0.26	-14.45	0.54	-12.45	0.57
Pyroxene-TiO_2=8.3	Area 2	Blocky w/out spinel	-3.77	0.26	-14.48	0.54	-12.51	0.57
Pyroxene-TiO_2=9.7	Area 2	Blocky w/out spinel	-5.95	0.26	-17.92	0.54	-14.82	0.57
Pyroxene-TiO_2=8.8	Area 3	Blocky w/out spinel	-11.08	0.30	-28.15	0.49	-22.39	0.54
Pyroxene-TiO_2=9.4	Area 3	Blocky w/out spinel	-11.76	0.30	-28.11	0.49	-22.00	0.54
Pyroxene-TiO_2=10.5	Area 4	Blocky w/out spinel	-6.95	0.30	-21.21	0.49	-17.59	0.54
Pyroxene-TiO_2=12.0	Area 4	Blocky w/out spinel	-6.44	0.30	-19.96	0.49	-16.61	0.54
Pyroxene-TiO_2=8.0	Area 5	Blocky w/out spinel	-11.58	0.30	-27.93	0.49	-21.91	0.54

* Pyroxene TiO_2 contents are in weight percent.